Application of Dynamic Fracture Mechanics Concepts to Composites: Final Report 2000

by

J.J. Mason

Department of Aerospace and Mechanical Engineering
University of Notre Dame

Notre Dame, Indiana 46556
January, 2000

20000209 176

Structural/Solid Mechanics
Laboratory Report No. 00/1

Application of Dynamic Fracture Mechanics Concepts to Composites: FINAL REPORT 2000

J.J. Mason [1]
Department of Aerospace and Mechanical Engineering
University of Notre Dame
Notre Dame, IN 46556

June, 1999

[1] Associate Professor, Principal Investigator

Abstract

This report summarizes the work completed in the months of June 1996–December 1999 for the principal investigator's Young Investigator Program grant. As such the report represents a final summary of work and is organized as follows. First, in a brief summary chapter, a review of the accomplishments of the work supported from June 1996 to December 1999 is given providing an overview of the successes during that period. Next, two chapters giving details of new work during the six months since the last annual report are presented. In these results an experimentally useful solution for the stress intensity factor history at the corner of an impacting punch is derived for isotropic and orthotropic materials. Then that solution is compared to an experiment using interferometry to measure the stress intensity factor history at the corner of an impacting punch in both isotropic and anisotropic materials. Good agreement between the model and the experiments is seen. Consequently, it is concluded that the solutions derived throughout the duration of this work are accurate—mathematically speaking the fundamental solutions are actually exact—and describe the loading under blunt impact quite well. With such accurate descriptions of the stress in the material under impact, future work can now focus on understanding the failure in the material under these same conditions.

Contents

Chapter 1

Summary of Accomplishments

An analytical approach to blunt impact problems on isotropic and anisotropic materials using dynamic fracture mechanics was shown to be valid over the duration of the grant. This approach used the mathematical and experimental techniques usually associated with dynamic fracture mechanics to examine impact of a blunt object on a wide class of materials. For simplicity sake, situations were limited to two-dimensional loading and geometries. Although this offers some limitations on the results, it also allows both the derivation of exact solutions describing events occurring on the interior of impacted materials *and* the experimental observation of those events, neither of which is readily achieved for three-dimensional problems. In addition, the two-dimensional results offer useful insight into three-dimensional impact events and provide valuable intuition about such events.

1.1 Previously Reported Work

First, through studies of impact on metals, it was shown in this work that fracture toughness can be used to characterize failure of metals by shear localization under impact conditions. Simple solutions for the stress intensity factor in the dynamic punch test were derived using known fundamental solutions from dynamic fracture mechanics. The results of these models were published as

> K.M. Roessig and J.J. Mason, "Dynamic Stress Intensity Factors in a Two Dimensional Punch Test," *Engineering Fracture Mechanics,* **60**, No. 4, pp 421-435,

1998

The conclusion from the models was that the stress intensity history around the corner of an impacting punch was more severe than that around a notch tip in a Kalthoff test. This result was significant in light of the fact that much attention has been directed toward the Kalthoff test as a measure of resistance to shear localization during impact. As it was shown by the model, actual impact can be worse than the Kalthoff test.

The solution for the stress intensity factor history around the corner of a punch impacting on an isotropic material was then used to test many types of metals. It was seen that shear band initiation at the corner of a punch was quite similar to that seen at a notch tip and that initiation occurred at the same value of stress intensity factor in both cases. These results were quite surprising but none-the-less lead one to believe that a fracture mechanics approach to modeling shear localization may be possible. The results were published as

> K.M. Roessig and J.J. Mason, "Adiabatic Shear Localization in the Impact of Edge Notched Specimens," *Experimental Mechanics*, **38**, No. 3, pp. 196-203, 1998

After examining isotropic materials, attention was turned to anisotropic materials and solutions for stress intensity factors in two dimensional orthotropic materials were derived. Initially, solutions using numerical methods were found. This approach involved reducing the governing equations (in this case the conservation of momentum in terms of displacement) to a Fredholm integral equation for the Laplace transform of the stress intensity factor history. Although numerical inversion of the Laplace transform, found by solving the Fredholm equation numerically, can be tricky, it was successfully performed for the case of normal and shear point loads applied to a finite crack. These results were published separately; the results for normal loads appeared as

> C. Rubio-Gonzalez and J.J. Mason, "Green's Functions for the Stress Intensity Factor Evolution in Finite Cracks in Orthotropic Materials," *to appear Int. J.*

4

and the results for shear point loads appeared as

> C. Rubio-Gonzalez and J.J. Mason, "Response of Finite Cracks in Orthotropic
> Materials due to Concentrated Impact Shear Loads," *J. Applied Mechanics*, **66**,
> no. 2, pp. 485-491,1999

Once the problems for finite cracks had been solved it was discovered that instead of reducing the governing equations to a Fredholm integral equation, one could reduce them to a Weiner-Hopf equation. This is quite an advance in the analysis techniques for dynamic fracture. When studying isotropic materials, it is common to reduce important, fundamental problems to a Weiner-Hopf equation by using Helmholtz displacement potentials. Using a similar technique on anisotropic materials was not possible because proper Helmholtz potentials do not exist for anisotropic materials; they only exist for isotropic materials. Here, however, we were able to reduce the governing equations for displacements to a Weiner-Hopf equation directly, without the use of displacement potentials. Hence, a whole new class of fundamental problems in dynamic fracture mechanics could be solved. We published a summary of our method, as it is applied to uniformly loaded, semi-infinite cracks in orthotropic materials, in the prestigious *Journal of Mechanics and Physics of Solids*as

> C. Rubio-Gonzalez and J.J. Mason, "Closed Form Solutions for the Dynamic
> Stress Intensity Factor at the Tip of Uniformly Loaded Semi-infinite Cracks in
> Orthotropic Materials," *to appear J. Mechanics and Physics of Solids, 1998*

Then we looked at point loads applied to semi-infinite cracks in orthotropic materials. These closed form solutions serve as Green's functions for solutions to a wide class of problems and differ from our earlier numerical solutions in that they are closed form and apply to semi-infinite cracks rather than finite cracks. The new method of reducing the problem to a Weiner-Hopf equations was used to find solutions for normal point loads, published as as

C. Rubio-Gonzalez and J.J. Mason, "Dynamic Stress Intensity Factor Due to Concentrated Normal Loads on Semi-infinite Cracks in Orthotropic Materials," *to appear Journal of Composite Materials, 1999*

and shear point loads, published as

C. Wang, C. Rubio-Gonzalez and J.J. Mason, "Dynamic Stress Intensity Factor on Semi-infinite Cracks in Orthotropic Materials Due to Concentrated Shear Impact Loads," *submitted to Int. J. of Solids and Structures, 1998.*

These solution, in contrast to the solutions described in the preceding paragraph, are closed form and not nearly as tricky to evaluate numerically. Next, we turned our attention to propagating cracks. The same method allowed us to find two approximations which describe the variation of the stress intensity factor as a function of crack velocity, one for isotropic materials that agreed with known solutions and one for highly orthotropic materials that contributed new knowledge in the area of dynamic fracture. This work was published as

C. Rubio-Gonzalez and J.J. Mason, "Dynamic Stress Intensity Factor for a Propagating Semi-Infinite Crack in Orthotropic Materials," *to appear Int. J. of Engineering Science, 1998.*

Such results are useful in characterizing material resistance to dynamic crack propagation.

Having found a new mathematical technique for solving two dimensional dynamic fracture problems in orthotropic materials, we attempted to apply the technique to quasi-three-dimensional problems. We examined the loading of penny shaped cracks in transversely isotropic materials. Using an approach based on the approach derived for two-dimensional problems, we were able to approximate the penny shaped crack problem by a simpler problem that could be reduced to a system of two Weiner-Hopf equations. This problem was solved and the results show how a penny shaped crack might grow if it were loaded dynamically in tension or shear. The paper resulting from the analysis is published as

C.Y. Wang and J.J. Mason, "The Dynamic Stress Intensity Factor and Strain Energy Release Rate for a Semi-infinite Crack in Rotated Transversely Isotropic Materials due to Uniform Impact Loading," *submitted to Int. J. of Fracture, 1999.*

This results is useful when studying the initiation of delaminations in composites under impact loading.

1.2 Recent Work

Finally, during the last six months of the funded effort, experimental investigation of the application of the solutions for stress intensity factors in orthotropic materials to dynamic crack initiation in composites under impact conditions was completed. First, the fundamental solutions derived for semi-infinite cracks in orthotropic materials were used to calculate the stress intensity factor in the dynamic punch test. This work is presented in Chapter 2 and has been submitted as

C. Rubio-Gonzalez and J.J. Mason, "Elastodynamic Analysis of Finite Punch and Finite Crack Problems in Orthotropic Materials," *submitted to Theoretical and Applied Fracture Mechanics, 1999*

With that solution in hand, we performed experiments on isotropic and orthotropic materials and measured the stress intensity factor history in the dynamic punch tests. This work is presented in Chapter 3 and published as

C. Rubio-Gonzalez and J.J. Mason, "Experimental Investigation of Dynamic Punch Tests on Isotropic and Composite Materials," *submitted to Experimental Mechanics, 1999*

The results agree quite well with the solution in Chapter 2 and thus verify solutions presented here and the method used to derive them.

1.3 Summary of Journal Publications

Overall, the work has been quite successful and has lead to significant advances in the modeling of dynamic fracture in anisotropic materials. A total of eleven journal publications have been produced and fifteen conference presentations and invited lectures have been given by the principal investigator. Also, two students have received their Ph.D. degrees; one from an under-represented group in engineering. Future work should be directed toward using these solutions in experimental investigation of material resistance to fracture under dynamic loading conditions such as underwater blasts or fragment impact.

The following list gives the journal publications resulting from the funded work.

1. C. Rubio-Gonzalez and J.J. Mason, "Elastodynamic Analysis of Finite Punch and Finite Crack Problems in Orthotropic Materials," *submitted to Theoretical and Applied Fracture Mechanics, 1999*

2. C. Rubio-Gonzalez and J.J. Mason, "Experimental Investigation of Dynamic Punch Tests on Isotropic and Composite Materials," *submitted to Experimental Mechanics, 1999*

3. C.Y. Wang and J.J. Mason, "The Dynamic Stress Intensity Factor and Strain Energy Release Rate for a Semi-infinite Crack in Rotated Transversely Isotropic Materials due to Uniform Impact Loading," *submitted to Int. J. of Fracture, 1999*

4. C. Wang, C. Rubio-Gonzalez and J.J. Mason, "Dynamic Stress Intensity Factor on Semi-infinite Cracks in Orthotropic Materials Due to Concentrated Shear Impact Loads," *submitted to Int. J. of Solids and Structures, 1998*

5. C. Rubio-Gonzalez and J.J. Mason, "Dynamic Stress Intensity Factor for a Propagating Semi-Infinite Crack in Orthotropic Materials," *to appear Int. J. of Engineering Science, 1998*

6. C. Rubio-Gonzalez and J.J. Mason, "Dynamic Stress Intensity Factor Due to Concentrated Normal Loads on Semi-infinite Cracks in Orthotropic Materials," *to appear Journal of Composite Materials, 1998*

7. C. Rubio-Gonzalez and J.J. Mason, "Closed Form Solutions for the Dynamic Stress Intensity Factor at the Tip of Uniformly Loaded Semi-infinite Cracks in Orthotropic Materials," *to appear J. Mechanics and Physics of Solids, 1998*

8. C. Rubio-Gonzalez and J.J. Mason, "Green's Functions for the Stress Intensity Factor Evolution in Finite Cracks in Orthotropic Materials," *to appear Int. J. Fracture, 1999*

9. C. Rubio-Gonzalez and J.J. Mason, "Response of Finite Cracks in Orthotropic Materials due to Concentrated Impact Shear Loads," *J. Applied Mechanics,* **66**, no. 2, pp. 485-491,1999

10. K.M. Roessig and J.J. Mason, "Adiabatic Shear Localization in the Impact of Edge Notched Specimens," *Experimental Mechanics,* **38**, No. 3, pp. 196-203, 1998

11. K.M. Roessig and J.J. Mason, "Dynamic Stress Intensity Factors in a Two Dimensional Punch Test," *Engineering Fracture Mechanics,* **60**, No. 4, pp 421-435, 1998

Chapter 2

Elastodynamic Analysis of Finite Punch and Finite Crack Problems in Orthotropic Materials

Overview

The transient elastodynamic response of the finite punch and finite crack problems in orthotropic materials is examined. Solution for the stress intensity factor history around the punch corner and crack tip is found. Laplace and Fourier transforms together with the Wiener-Hopf technique are employed to solve the equations of motion in terms of displacements. A detailed analysis is made in the simplified case when a flat rigid punch indents an elastic orthotropic half-plane, the punch approaches with a constant velocity normally to the boundary of the half-plane. An asymptotic expression for the singular stress near the punch corner is analyzed leading to an explicit expression for the dynamic stress intensity factor which is valid for the time the dilatational wave takes to travel twice the punch width. In the crack problem, a finite crack is considered in an infinite orthotropic plane. The crack faces are loaded by impact uniform pressure in mode I. An expression for the dynamic stress intensity factor is found which is valid while the dilatational wave travels the crack length twice. Results for orthotropic materials are shown to converge to known solutions for isotropic materials derived independently.

2.1 Introduction

The punch problem is of great importance in solid mechanics for its multiple technical applications including ballistic impact, explosives, metal forming and manufacturing operations such as punching and blanking. While the quasi-static punch problem is a well studied field in contact mechanics [1, 2], there is little work on the dynamic case. In the dynamic case the punch approaches the material with a certain velocity, hence wave propagation is involved complicating the mathematical analysis.

Brock [3, 4] considered the problem of a rapid indentation of an isotropic half-plane by a smooth, flat and rigid semi-infinite punch. The high stresses generated under the punch edge were assumed to generate slip mechanisms, and the zone was allowed to relax the stresses

under the punch edge. That is, the stress relaxation feature of the zone was imposed to remove the square-root singularity in the normal contact stress under the punch edge, and this condition led to simplify the mathematical treatment. It has been shown, however, in a series of experiments conducted in isotropic and unidirectional composite materials [5], that such plastic zone is small enough like that usually assumed near a crack tip in fracture mechanics, and the singular stress field prevails near the punch edge. In those experiments, a rigid flat projectile with sharp corners impacted (at moderate velocities ≈ 20 m/s) one side of rectangular specimens, and the stress intensity factor time evolution, which is a parameter related to the singular normal stress near the punch edge, was measured using the laser interferometry method of coherent gradient sensor (CGS method), in combination with high speed photography.

Punch geometries other than flat, have been considered even for general anisotropic materials, e.g. parabolic and wedge shaped punches, [6, 7]. In those problems the contact area grows at constant speed and the self-similar feature of the dynamic fields is exploited using the general methodology derived by Willis [6] for such kind of problems.

The dynamic, flat *finite* punch problem of width $2l$ in isotropic materials was considered by Roessig and Mason[8]. They solved an equivalent problem where the rigid punch is replaced by a compressive wave impinging two semi-infinite external cracks. The computation of the stress intensity factor history for the time interval $0 < t < 4l/c_d$, was carried out by integration of a Green's function in space and time. The appropriate Green's function is the solution derived by Freund [9] for the semi-infinite crack problem with impact point loads applied normally on the crack faces at certain distance l_p from the crack tip. Even though this procedure may be extended for the case of orthotropic materials, since the needed Green's function has been developed by Rubio-Gonzalez and Mason [10], another approach will be used in this work. A procedure similar to that presented by Poruchikov [11] is employed here which allows the determination of an explicit expression for the stress intensity factor history in the time interval $0 < t < 4l/c_d$.

In the following, the semi-infinite and finite punch problems are considered. A more general semi-infinite punch problem is solved first where a non-homogeneous boundary condition outside the punch is allowed. This strategy will permit to construct a solution for the finite punch problem as a superposition of semi-infinite punch solutions. The expression for the dynamic stress intensity factor in the *finite* punch problem in orthotropic materials is new in the literature. The dynamic stress intensity factor for the semi-infinite punch coincides with that for the semi-infinite crack under uniform impact loads on the crack faces in mode I and it was derived first in [12].

The same strategy is applied then to construct a solution for the finite crack problem in orthotropic materials. The stress intensity factor history $K_I(t)$ is determined for the time interval $0 < t < 4l/c_d$, being $2l$ the crack length. The dynamic crack problem in orthotropic materials was considered first by Bandyopahya and Kassir [13] using a method derived by Chen and Sih [14]. Such method gives an approximate solution for $K_I(t)$ after performing a numerical solution of a Fredholm integral equation and numerical Laplace transform inversion. Nevertheless this method permits the determination of $K_I(t)$ for long times, it may be inaccurate if the proper numerical schemes are not selected, as will be illustrated in this work comparing Kassir and Banyopadhyay [13] results with the exact solution developed here. The Wiener-Hopf technique has been applied in the finite crack problems in isotropic materials [15, 16]. Freund [16] developed an expression for the dynamic stress intensity factor using a fundamental solution for a moving dislocation which is a different approach to that used in this work. It is noted that Freund's solution for the isotropic case is recovered from the orthotropic expression developed here with the proper substitution of the elastic constants.

2.2　Semi-infinite Punch

2.2.1　Governing Equations

Consider that at $t = 0$ a smooth punch begins its indentation into an elastic orthotropic half-plane $y \geq 0$, at a semi-infinite interval $x \geq 0$ of its boundary, see figure 2.1. Let E_i, μ_{ij} and ν_{ij} $(i, j = 1, 2, 3)$ be the engineering elastic constants of the material where the indices 1, 2, and 3 correspond to the directions (x, y, z) of a system of Cartesian coordinates chosen to coincide with the axes of material orthotropy.
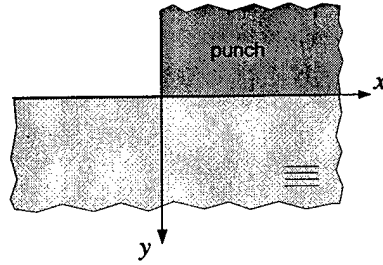

Figure 2.1: Schematic of the semi-infinite punch.

The problem is restricted to two dimensions with wave propagation in the $x - y$ plane only. By setting all the derivatives with respect to z to be zero, it is readily shown that the displacement equations of motion [17] reduce to

$$c_{11}\frac{\partial^2 u}{\partial x^2} + \frac{\partial^2 u}{\partial y^2} + (1 + c_{12})\frac{\partial^2 v}{\partial x \partial y} = \frac{1}{c_s^2}\frac{\partial^2 u}{\partial t^2}, \qquad (2.1)$$

$$\frac{\partial^2 v}{\partial x^2} + c_{22}\frac{\partial^2 v}{\partial y^2} + (1 + c_{12})\frac{\partial^2 u}{\partial x \partial y} = \frac{1}{c_s^2}\frac{\partial^2 v}{\partial t^2}, \qquad (2.2)$$

where u and v are the x and y components of the displacement vector and c_{11}, c_{12} and c_{22} are non-dimensional parameters related to the elastic constants by the relations:

$$
\begin{aligned}
c_{11} &= \frac{E_1}{\mu_{12}[1 - (E_2/E_1)\nu_{12}^2]}, \\
c_{22} &= (E_2/E_1)c_{11}, \\
c_{12} &= \nu_{12}c_{22} = \nu_{21}c_{11},
\end{aligned}
\qquad (2.3)
$$

14

for generalized plane stress, and by

$$
\begin{aligned}
c_{11} &= \frac{E_1}{\mu_{12}\Delta}(1 - \nu_{23}\nu_{32}), \\
c_{22} &= \frac{E_2}{\mu_{12}\Delta}(1 - \nu_{13}\nu_{31}), \\
c_{12} &= \frac{E_1}{\mu_{12}\Delta}(\nu_{21} + \frac{E_2}{E_1}\nu_{13}\nu_{32}), \\
\Delta &= 1 - \nu_{12}\nu_{21} - \nu_{23}\nu_{32} - \nu_{31}\nu_{13} - \nu_{12}\nu_{23}\nu_{31} - \nu_{13}\nu_{21}\nu_{32},
\end{aligned}
\tag{2.4}
$$

for plane strain. In the orthotropic solid, $c_s = \sqrt{\mu_{12}/\rho}$ represents the velocity of the in-plane shear wave propagating along the the principal material axes and ρ is the mass density. The stresses are related to the displacements by the equations:

$$
\begin{aligned}
\frac{\sigma_x}{\mu_{12}} &= c_{11}\frac{\partial u}{\partial x} + c_{12}\frac{\partial v}{\partial y}, \\
\frac{\sigma_y}{\mu_{12}} &= c_{12}\frac{\partial u}{\partial x} + c_{22}\frac{\partial v}{\partial y}, \\
\frac{\tau_{xy}}{\mu_{12}} &= \frac{\partial u}{\partial y} + \frac{\partial v}{\partial x}.
\end{aligned}
\tag{2.5}
$$

2.2.2 Method of Solution

Let $f_0(x, t)$ be a function describing the motion of the punch. Thus the boundary conditions are

$$
\begin{aligned}
\sigma_y(x, 0, t) &= 0 \quad \text{for} \quad -\infty < x < 0, \\
\tau_{xy}(x, 0, t) &= 0 \quad \text{for} \quad -\infty < x < \infty, \\
v(x, 0, t) &= f_0(x, t) \quad \text{for} \quad x \geq 0.
\end{aligned}
\tag{2.6}
$$

In addition, the condition of zero displacements at infinity and zero initial conditions are assumed. Note that the first two equations in (2.6) indicate that the boundary $y = 0$ outside the punch is stress free. To ensure the uniqueness of the solution [11] it is necessary to restrict the behavior of the displacement in the vicinity of the edge of the punch ($x = 0$), that is,

$$
v(x, y, t) = \bar{v}(t) + O(r^\epsilon), \quad \epsilon > 0, \quad r \to 0, \quad (r = \sqrt{x^2 + y^2}).
\tag{2.7}
$$

Instead of solving the problem with the homogeneous boundary condition $\sigma_y(x,0,t) = 0$ in equations (2.6), consider a more general problem with a given non-homogeneous boundary condition $\sigma_y(x,0,t) = \sigma_-(x,t)$ for $x < 0$, *i.e.*, equations (2.6) become

$$\sigma_y(x,0,t) = \sigma_-(x,t) \qquad \text{for} \quad -\infty < x < 0,$$

$$\tau_{xy}(x,0,t) = 0 \qquad \text{for} \quad -\infty < x < \infty, \qquad (2.8)$$

$$v(x,0,t) = f_0(x,t) \qquad \text{for} \quad x \geq 0,$$

where $\sigma_-(x,t)$ is assumed to be equal to zero at any $x < -c_d t - k$ ($k \geq 0$). The new problem with boundary conditions (2.8) will be useful in solving dynamic problems with the finite punch. Note that with $\sigma_-(x,t) \equiv 0$ the standard problem with the semi-infinite punch is recovered. The function $\sigma_-(x,t)$ is limited everywhere except for the point $x = 0$ where it should satisfy the constraint

$$\sigma_-(x,t) = O(x^{-1+\epsilon}), \qquad \epsilon > 0, \qquad x \to 0^-. \qquad (2.9)$$

The method of solution of the governing equations presented here follows that described by Poruchikov [11] for the isotropic case with some significant differences. Displacement potentials are not used. In equations (2.1) and (2.2), the time variable may be removed by application of the Laplace transform

$$f^*(p) = \int_0^\infty f(t)\, e^{-pt}\, dt, \qquad f(t) = \frac{1}{2\pi i} \int_{Br} f^*(p)\, e^{pt}\, dt, \qquad (2.10)$$

where Br denotes the Bromwich path of integration which is a line parallel to the imaginary axis in the p-plane. Applying relations (2.10) to equations (2.1) and (2.2) and using zero initial conditions for the displacements and velocities, the transformed field equations become

$$c_{11}\frac{\partial^2 u^*}{\partial x^2} + \frac{\partial^2 u^*}{\partial y^2} + (1+c_{12})\frac{\partial^2 v^*}{\partial x \partial y} - \frac{p^2}{c_s^2}u^* = 0, \qquad (2.11)$$

$$\frac{\partial^2 v^*}{\partial x^2} + c_{22}\frac{\partial^2 v^*}{\partial y^2} + (1+c_{12})\frac{\partial^2 u^*}{\partial x \partial y} - \frac{p^2}{c_s^2}v^* = 0, \qquad (2.12)$$

where the transformed displacement components, u^* and v^*, are now functions of the variables x, y, and p. The application of the Laplace transform to the boundary conditions (2.8)

16

gives

$$\sigma_y^*(x, 0, p) = \sigma_-^*(x, p) \quad \text{for} \quad -\infty < x < 0,$$

$$\tau_{xy}^*(x, 0, p) = 0 \quad \text{for} \quad -\infty < x < \infty, \tag{2.13}$$

$$v^*(x, 0, p) = f_0^*(x, p) \quad \text{for} \quad x > 0.$$

To obtain a solution of the differential equations (2.11) and (2.12) subject to conditions (2.13), the Fourier transform is applied,

$$F(s) = \int_{-\infty}^{\infty} f(x) \, e^{isx} \, dx, \quad f(x) = \frac{1}{2\pi} \int_{-\infty}^{\infty} F(s) \, e^{-isx} \, ds. \tag{2.14}$$

It is assumed that the displacements in the Laplace transform domain have the form

$$u^*(x, y, p) = \frac{1}{2\pi} \int_{-\infty}^{\infty} A(s, y, p) e^{-isx} \, ds, \tag{2.15}$$

$$v^*(x, y, p) = \frac{1}{2\pi} \int_{-\infty}^{\infty} B(s, y, p) e^{-isx} \, ds, \tag{2.16}$$

where A and B are the Fourier transforms of the Laplace transform of the displacements, u^* and v^*, respectively, and are yet to be determined. Substituting these transforms into equations (2.11) and (2.12), the functions A and B are found to satisfy the simultaneous ordinary differential equations

$$(c_{11}s^2 + p^2/c_s^2)A - \frac{d^2 A}{dy^2} + (1 + c_{12})is\frac{dB}{dy} = 0, \tag{2.17}$$

$$(s^2 + p^2/c_s^2)B - c_{22}\frac{d^2 B}{dy^2} + (1 + c_{12})is\frac{dA}{dy} = 0. \tag{2.18}$$

The solution of these equations which vanishes for $y \to \infty$ is

$$A(s, y, p) = A_1(s, p)e^{-\gamma_1 y} + A_2(s, p)e^{-\gamma_2 y},$$

$$B(s, y, p) = \frac{-i\alpha_1}{s}A_1(s, p)e^{-\gamma_1 y} - \frac{i\alpha_2}{s}A_2(s, p)e^{-\gamma_2 y}, \tag{2.19}$$

where A_1 and A_2 are arbitrary functions and $\alpha_j(s, p)$ stands for the functions

$$\alpha_j(s, p) = \frac{c_{11}s^2 + p^2/c_s^2 - \gamma_j^2}{(1 + c_{12})\gamma_j}, \quad j = 1, 2 \tag{2.20}$$

17

with γ_1^2 and γ_2^2 being two distinct roots of the quadratic equation

$$c_{22}\gamma^4 + [(c_{12}^2 + 2c_{12} - c_{11}c_{22})s^2 - (1 + c_{22})p^2/c_s^2]\gamma^2 + (c_{11}s^2 + p^2/c_s^2)(s^2 + p^2/c_s^2) = 0. \quad (2.21)$$

The branches of $\gamma_1(p, s)$ and $\gamma_2(p, s)$ are chosen in the appropriate Riemann sheets and having positive real parts. It has been shown by Willis (1973) and Poruchikov (1993) that such a restriction on γ_1 and γ_2 is possible for the general anisotropic case as long as $\text{Re}\{p\} > 0$. This fact is a consequence of the positive definiteness of the strain energy. The expressions for the displacements in the Laplace transform domain become:

$$u^* = \frac{1}{2\pi} \int_{-\infty}^{\infty} (A_1 e^{-\gamma_1 y} + A_2 e^{-\gamma_2 y})e^{-isx}\, ds, \quad (2.22)$$

$$v^* = \frac{-i}{2\pi} \int_{-\infty}^{\infty} (\alpha_1 A_1 e^{-\gamma_1 y} + \alpha_2 A_2 e^{-\gamma_2 y})\frac{e^{-isx}}{s}ds, \quad (2.23)$$

and using (2.5) the corresponding expression for τ_{xy}^* is given by

$$\tau_{xy}^* = -\frac{\mu_{12}}{2\pi} \int_{-\infty}^{\infty} [(\alpha_1 + \gamma_1)A_1 e^{-\gamma_1 y} + (\alpha_2 + \gamma_2)A_2 e^{-\gamma_2 y}]e^{-isx}\, ds. \quad (2.24)$$

Applying the second condition of (2.13) to equation (2.24) yields

$$A_2(s,p) = -\beta_1 A_1(s,p),$$

$$\beta_1 = \frac{\alpha_1 + \gamma_1}{\alpha_2 + \gamma_2}. \quad (2.25)$$

Therefore, the expressions for the transformed components of displacement become

$$u^*(x,y,p) = \frac{1}{2\pi} \int_{-\infty}^{\infty} (e^{-\gamma_1 y} - \beta_1 e^{-\gamma_2 y})A_1(s,p)e^{-isx}\, ds, \quad (2.26)$$

$$v^*(x,y,p) = \frac{-i}{2\pi} \int_{-\infty}^{\infty} (\alpha_1 e^{-\gamma_1 y} - \beta_1 \alpha_2 e^{-\gamma_2 y})\frac{A_1(s,p)}{s}e^{-isx}\, ds, \quad (2.27)$$

and the associated stress components are given by

$$\sigma_x^* = \frac{-i\mu_{12}}{2\pi} \int_{-\infty}^{\infty} [(c_{11}s^2 - \alpha_1\gamma_1 c_{12})e^{-\gamma_1 y} - (c_{11}s^2 - \alpha_2\gamma_2 c_{12})\beta_1 e^{-\gamma_2 y}]\frac{A_1(s,p)}{s}e^{-isx}ds, \quad (2.28)$$

$$\sigma_y^* = \frac{-i\mu_{12}}{2\pi} \int_{-\infty}^{\infty} [(c_{12}s^2 - \alpha_1\gamma_1 c_{22})e^{-\gamma_1 y} - (c_{12}s^2 - \alpha_2\gamma_2 c_{22})\beta_1 e^{-\gamma_2 y}]\frac{A_1(s,p)}{s}e^{-isx}ds, \quad (2.29)$$

$$\tau_{xy}^* = \frac{-\mu_{12}}{2\pi} \int_{-\infty}^{\infty} (\alpha_1 + \gamma_1)[e^{-\gamma_1 y} - e^{-\gamma_2 y}]A_1(s,p)e^{-isx}ds. \quad (2.30)$$

The following functions are introduced,

$$E(s,p) = \frac{1}{s}(\alpha_1 - \beta_1\alpha_2)A_1(s,p), \tag{2.31}$$

$$F(s,p) = -\frac{\sqrt{s^2 + p^2/c_d^2}}{(\alpha_1 - \beta_1\alpha_2)\xi}[c_{12}s^2 - \alpha_1\gamma_1 c_{22} - \beta_1(c_{12}s^2 - \alpha_2\gamma_2 c_{22})], \tag{2.32}$$

$$\xi = \frac{\beta\sqrt{\frac{c_{22}}{c_{11}}}}{\sqrt{\beta - 2\frac{c_{12}}{c_{22}} + 2\sqrt{\frac{c_{11}}{c_{22}}}}}, \tag{2.33}$$

$$\beta = \frac{c_{11}c_{22} - c_{12}^2}{c_{22}}, \tag{2.34}$$

where the velocity $c_d = \sqrt{c_{11}}c_s$ represents the dilatational wave speed along the $x-$axis. In view of the first and third boundary conditions in (2.13), equation (2.27) and (2.29) now yield the following pair of dual integral equations for the determination of the function $E(s,p)$

$$\sigma_y^*(x,0,p) = \frac{i\mu_{12}\xi}{2\pi}\int_{-\infty}^{\infty}\frac{F(s,p)}{\sqrt{s^2 + p^2/c_d^2}}E(s,p)e^{-isx}\,ds = \sigma_-^*(x,p) \qquad -\infty < x < 0, \tag{2.35}$$

$$v^*(x,0,p) = \frac{-i}{2\pi}\int_{-\infty}^{\infty}E(s,p)e^{-isx}\,ds = f_0^*(x,p) \qquad 0 < x < \infty, \tag{2.36}$$

Let $v_-^*(x,p)$ be the unknown Laplace transform of the vertical displacement on the negative $x-$axis, and $\sigma_+^*(x,p)$ be the unknown Laplace transform of the normal stress on the positive $x-$axis, so that

$$v^*(x,0,p) = \begin{cases} f_0^*(x,p) & \text{for} \quad x > 0 \\ v_-^*(x,p) & \text{for} \quad x < 0, \end{cases} \qquad \sigma_y^*(x,0,p) = \begin{cases} \sigma_+^*(x,p) & \text{for} \quad x > 0 \\ \sigma_-^*(x,p) & \text{for} \quad x < 0, \end{cases} \tag{2.37}$$

then we can write the Laplace transform of the normal stress and the vertical displacement on the whole boundary $y = 0$ as

$$\frac{i\mu_{12}\xi}{2\pi}\int_{-\infty}^{\infty}\frac{F(s,p)}{\sqrt{s^2 + p^2/c_d^2}}E(s,p)e^{-isx}\,ds = \sigma_-^*(x,p) + \sigma_+^*(x,p), \tag{2.38}$$

$$\frac{-i}{2\pi}\int_{-\infty}^{\infty}E(s,p)e^{-isx}\,ds = v_-^*(x,p) + f_0^*(x,p), \tag{2.39}$$

and by Fourier transform inversion, these equations give

$$i\mu_{12}\xi\frac{F(s,p)}{\sqrt{s^2 + p^2/c_d^2}}E(s,p) = \Sigma_-(s) + \Sigma_+(s), \tag{2.40}$$

$$-iE(s,p) = V_-(s) + V_+(s), \tag{2.41}$$

19

where

$$\Sigma_-(s) = \int_{-\infty}^0 \sigma_-^*(x,p)e^{isx}dx \qquad \Sigma_+(s) = \int_0^\infty \sigma_+^*(x,p)e^{isx}dx, \qquad (2.42)$$

$$V_-(s) = \int_{-\infty}^0 v_-^*(x,p)e^{isx}dx \qquad V_+(s) = \int_0^\infty f_0^*(x,p)e^{isx}dx, \qquad (2.43)$$

From a priori knowledge of properties of solutions of elastic wave equations it is possible to show that $\sigma_+^*(x,p)$ and $v_-^*(x,p)$ are exponentially bounded at infinity and this ensures the existence of their Fourier transform (2.42) and (2.43). The analysis is similar to that presented by Rubio-Gonzalez and Mason [12] for the crack problem. In addition it is shown by Noble [18] that

if $|\sigma_+^*(x,p)| < M_1 e^{\lambda_- x}$ as $x \to +\infty$ then $\quad \Sigma_+(s)$ is analytic in $\text{Im}(s) = \lambda > \lambda_-$,

and if $|v_-^*(x,p)| < M_2 e^{\lambda_+ x}$ as $x \to -\infty$ then $\quad V_-(s)$ is analytic in $\text{Im}(s) = \lambda < \lambda_+$.

Since all disturbances are, at least limited when $x \to +\infty$ and are absent if $x < -c_d t - k$, then $\sigma_+^*(x,p) \sim O(1)$ as $x \to +\infty$ and $v_-^*(x,p) \sim O(e^{px/c_d})$ as $x \to -\infty$. Therefore, it is possible to show that $\lambda_- = 0$ and $\lambda_+ = p/c_d$. Thus, the Fourier transforms (2.42) and (2.43) lead to conclude that $\Sigma_+(s)$ and $V_-(s)$ will be analytic in $\text{Im}(s) > 0$ and $\text{Im}(s) < p/c_d$ respectively.

2.2.3 Wiener-Hopf technique

Eliminating $E(s,p)$ from (2.40) and (2.41) we obtain a Wiener-Hopf equation

$$\Sigma_-(s) + \Sigma_+(s) = -\mu_{12}\xi\frac{F(s,p)}{\sqrt{s^2 + p^2/c_d^2}}[V_-(s) + V_+(s)] \qquad (2.44)$$

which contains only the two unknown functions $\Sigma_+(s)$ and $V_-(s)$, and now the Wiener-Hopf technique can be applied as follows. Suppose that the function $L(s)$ is defined and factored as

$$L(s) = \frac{L_-(s)}{L_+(s)} = \mu_{12}\xi\frac{F(s,p)}{\sqrt{s^2 + p^2/c_d^2}} \qquad (2.45)$$

then equation (2.44) becomes

$$\Sigma_-(s)L_+(s) + \Sigma_+(s)L_+(s) = -L_-(s)V_-(s) - L_-(s)V_+(s). \qquad (2.46)$$

20

Assume that the function $D(s)$ is defined and decomposed as

$$D(s) = \Sigma_-(s)L_+(s) + L_-(s)V_+(s) \tag{2.47}$$

$$= D_+(s) + D_-(s),$$

then equation (2.46) becomes

$$D_+(s) + \Sigma_+(s)L_+(s) = -L_-(s)V_-(s) - D_-(s) = W(s). \tag{2.48}$$

The first member of this equation is analytic in the upper half of the $s-$plane $\text{Im}(s) > 0$ and the second member is analytic in the lower half of the $s-$plane $\text{Im}(s) < p/c_d$. Therefore, the regions of analyticity overlap. Using the Liouville's theorem to determine $W(s)$, solutions for $\Sigma_+(s)$ and $V_-(s)$ can be found.

After algebraic manipulation it is found that the function $F(s,p)$ reduces to

$$F(s,p) = \frac{1}{\xi\sqrt{c_{11}}\sqrt{c_{11}s^2 + p^2/c_s^2}(\gamma_1 + \gamma_2)(1 + c_{12})}\Big\{ c_{22}c_{12}\gamma_1^2\gamma_2^2 - \gamma_1\gamma_2(1 + c_{12})c_{12}^2 s^2 +$$

$$(c_{11}s^2 + p^2/c_s^2)\Big[c_{22}(\gamma_1^2 + \gamma_2^2) + \gamma_1\gamma_2(1 + c_{12})c_{22} +$$

$$s^2(c_{12} + c_{12}^2 - c_{11}c_{22}) - c_{22}p^2/c_s^2\Big]\Big\} \tag{2.49}$$

The only zeros of $F(s,p)$ are of the form $s = \pm ip/c_R$ where c_R is the Rayleigh wave speed. This can be seen by substituting $s = ip/v$ in $F(s,p)$, letting $F(s,p) = 0$ and dividing by the non-zero factors, then $F(ip/v, p) = 0$ reduces to

$$\sqrt{\frac{c_{22}}{c_{11}}}\left(\frac{c_{11}c_{22} - c_{12}^2}{c_{22}} - \frac{v^2}{c_s^2}\right)\sqrt{1 - \frac{v^2}{c_s^2}} - \frac{v^2}{c_s^2}\sqrt{1 - \frac{v^2}{c_{11}c_s^2}} = 0$$

which is the Rayleigh function for orthotropic materials [19]. The roots of this function are $v = \pm c_R$. For a proof that equation (2.49) has only these two zeros see [12]

Consequently, the first step in factoring $L(s)$ is to define

$$\hat{F}(s) = \frac{F(s,p)}{s^2 + p^2/c_R^2}. \tag{2.50}$$

It can be shown that $\hat{F}(s) \to 1$ as $s \to \infty$, (the constant ξ in (2.32) was chosen to make this possible). The function $\hat{F}(s)$ is regular and $\hat{F}(s) \neq 0$ in the $s-$plane cut as shown in figure
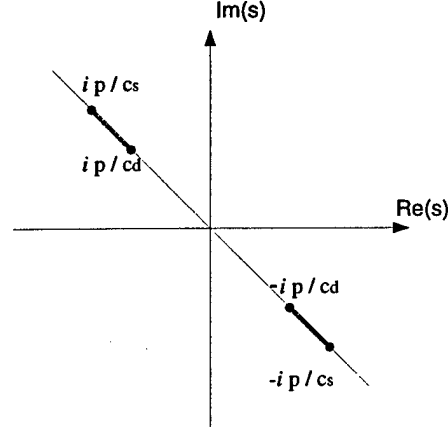
21

Figure 2.2: Branch cuts of $\hat{F}(s)$ in the s-plane.

2.2, the only singularities are the branch points shared with γ_1 and γ_2. Where the branch points of γ_1 and γ_2 are

$$\text{for } \gamma_1; \quad s = \pm\frac{ip}{c_s},$$

$$\text{for } \gamma_2; \quad s = \pm\frac{ip}{\sqrt{c_{11}}\, c_s} = \pm\frac{ip}{c_d}.$$

It is well-known that factorization is accomplished most directly for functions that approach unity as $|s| \to \infty$ and that have neither zeros nor poles in the finite plane; $\hat{F}(s)$ is an example of such a function. Therefore, using Cauchy's integral formula it can be shown that [16]

$$\hat{F}_\pm(s) = \exp\left\{\frac{1}{2\pi i}\int_{\Gamma_\pm}\frac{\log \hat{F}(z)}{z-s}\,dz\right\}$$

where $\hat{F}(s) = \hat{F}_+(s)\hat{F}_-(s)$ and Γ_- (Γ_+) is the contour enclosing the branch cut between $+ip/c_d$ and $+ip/c_s$, ($-ip/c_d$ and $-ip/c_s$). Using the fact that $\hat{F}(\bar{s}) = \overline{\hat{F}(s)}$, one can write

$$\hat{F}_\pm(s) = \exp\left\{\frac{-1}{\pi}\int_{1/c_d}^{1/c_s}\tan^{-1}\left(\frac{\text{Im}[\hat{F}(ipw)]}{\text{Re}[\hat{F}(ipw)]}\right)\frac{dw}{w \mp \frac{is}{p}}\right\}$$

Note that by making $s = ip\zeta$ in this equation, $\hat{F}_\pm(s = ip\zeta) = \tilde{F}_\pm(\zeta)$ becomes a function only of ζ. That is

$$\tilde{F}_\pm(\zeta) = \exp\left\{\frac{-1}{\pi}\int_{1/c_d}^{1/c_s}\tan^{-1}[R(w)]\frac{dw}{w \pm \zeta}\right\} \tag{2.51}$$

22

where

$$R(w) = \frac{\text{Im}[\hat{F}(ipw)]}{\text{Re}[\hat{F}(ipw)]}.$$

Returning to the factorization of $L(s)$ we have

$$L(s) = \frac{L_-(s)}{L_+(s)} = \mu_{12}\xi\frac{\hat{F}(s)(s^2 + p^2/c_R^2)}{\sqrt{s^2 + p^2/c_d^2}} \tag{2.52}$$

$$= \mu_{12}\xi\frac{\hat{F}_+(s)\hat{F}_-(s)(s + ip/c_R)(s - ip/c_R)}{\sqrt{s + ip/c_d}\sqrt{s - ip/c_d}} \tag{2.53}$$

therefore

$$L_-(s) = \mu_{12}\xi\frac{(s - ip/c_R)}{\sqrt{s - ip/c_d}}\hat{F}_-(s), \tag{2.54}$$

$$L_+(s) = \frac{\sqrt{s + ip/c_d}}{(s + ip/c_R)}\frac{1}{\hat{F}_+(s)}. \tag{2.55}$$

Using the sum splitting formula [18] for the function $D(s)$ defined in (2.47) it is found that

$$D_+(s) = \frac{1}{2\pi i}\int_{-\infty+i\lambda_0}^{\infty+i\lambda_0}\frac{D(z)}{z - s}dz, \tag{2.56}$$

$$D_-(s) = D(s) - D_+(s) \tag{2.57}$$

where λ_0 is such that $\lambda_- < \lambda_0 < \lambda_+$.

Each side of equation (2.48) is analytic in one of the overlapping half planes, and the sides coincide on the strip of overlap. Consequently each side of (2.48) is the analytic continuation of the other into its complementary half plane; so that the two sides together represent one and the same entire function $W(s)$. The entire function will be determined by its behavior at $|s| \to \infty$ which is related with the behavior of physical quantities near $x = 0$. First note that $L_+(s) \sim s^{-1/2}$ and $L_-(s) \sim s^{1/2}$ as $|s| \to \infty$. In addition, it may be proven, according with restrictions (2.7) and (2.9) that $\Sigma_-(s)$ and $V_+(s)$ vanish as $s \to 0$ in their respective planes of analyticity. Thus $D(s)$, $D_+(s)$ and $D_-(s)$ in (2.47), (2.56) and (2.57) are bounded in their respective planes of analyticity and vanish at infinity. Furthermore, $\sigma_+^*(x,p)$ is expected to be square root singular as $x \to 0^+$ and $v_-^*(x,p)$ is expected to vanish as $x \to 0^-$ to ensure

23

continuity of displacement. From the Abel theorem [18] relating asymptotic properties of transforms

$$\lim_{x \to 0^+} x^{1/2} \sigma_+^*(x, p) \sim \lim_{s \to \infty} s^{1/2} \Sigma_+(s)$$

$$\lim_{x \to 0^-} |x|^{-q} v_-^*(x, p) \sim \lim_{s \to -\infty} |s|^{1+q} V_-(s)$$

for some $q > 0$. Therefore, it is expected that $\Sigma_+(s) \sim s^{-1/2}$ and $V_-(s) \sim s^{-1-q}$ as $|s| \to \infty$, thus the products $\Sigma_+(s)L_+(s)$ and $L_-(s)V_-(s)$ vanish at infinity. Therefore, each side of (2.48) vanishes as $|s| \to \infty$ in the corresponding half planes. According the the Liouville's theorem, a bounded entire function is constant. In this case, $W(s)$ is bounded in the finite plane and $W(s) \to 0$ as $|s| \to \infty$ so that the constant must be zero; thus, $W(s) = 0$. By using (2.48) and (2.56), the functions of interest are then given by

$$\Sigma_+(s) = -\frac{D_+(s)}{L_+(s)} = -\frac{(s + ip/c_R)}{\sqrt{s + ip/c_d}} \hat{F}_+(s) D_+(s), \qquad (2.58)$$

$$V_-(s) = -\frac{D_-(s)}{L_-(s)} = -\frac{\sqrt{s - ip/c_d}}{\mu_{12}\zeta(s - ip/c_R)} \frac{D_-(s)}{\hat{F}_-(s)}. \qquad (2.59)$$

2.2.4 Semi-infinite smooth, rigid punch

Consider the special case of the standard semi-infinite punch (with boundary conditions given by (2.6)), thus $\sigma_-(x, t) \equiv 0$ and equation (2.42) gives $\Sigma_-(s) = 0$. Making further simplifications, assume the problem of a semi-infinite smooth, rigid punch such that $f_0(x, t) = f_0(t)$. Hence equation (2.43) gives $V_+(s) = f_0^*(p)/is$. Therefore (2.47) reduces to $D(s) = L_-(s)f_0^*(p)/is$ and its factorization follows easily

$$D(s) = L_-(s)\frac{f_0^*(p)}{is} = f_0^*(p)\left[\frac{L_-(s) - L_-(0)}{is} + \frac{L_-(0)}{is}\right], \qquad (2.60)$$

$$D_+(s) = f_0^*(p)\frac{L_-(0)}{is}. \qquad (2.61)$$

To find the stress intensity factor, an asymptotic expression for the normal stress near the punch edge is sought. The Abel's theorem which relates asymptotic expressions between

a function and its Fourier transform is used in combination with the definition of the stress intensity factor, that is, in the Laplace transform domain

$$K_I^*(p) = \lim_{x \to 0+} \sqrt{2\pi x}\, \sigma_+^*(x,p) = \lim_{s \to +\infty} e^{-i\pi/4} \sqrt{2s}\, \Sigma_+(s). \tag{2.62}$$

Substituting (2.54) in (2.61) and the result in (2.58) it is found that

$$\Sigma_+(s) = -\frac{(s + ip/c_R)}{\sqrt{s + ip/c_d}} \hat{F}_+(s) f_0^*(p) \frac{L_-(0)}{is}, \tag{2.63}$$

taking the limit when $s \to \infty$ and considering that

$$L_-(0) = \sqrt{-i} \mu_{12} \xi \frac{\sqrt{p}\sqrt{c_d}}{c_R} \hat{F}_-(0), \tag{2.64}$$

$\Sigma_+(s)$ becomes

$$\Sigma_+(s) = \frac{\mu_{12}\xi\sqrt{c_d}}{\sqrt{-i}c_R\sqrt{s}} \sqrt{p} f_0^*(p) \hat{F}_-(0) \quad \text{as } s \to \infty, \tag{2.65}$$

hence

$$K_I^*(p) = \sqrt{2}\frac{\mu_{12}\xi\sqrt{c_d}}{c_R} \sqrt{p} f_0^*(p) \hat{F}_-(0), \tag{2.66}$$

where $\hat{F}_-(0) = c_R\sqrt{\frac{\sqrt{c_{22}}}{c_s c_d \xi}}$.

Consider the case where the punch approaches the orthotropic half-plane with constant velocity v_0, then $f_0^*(p) = v_0/p^2 = \sigma_0/\rho\sqrt{c_{22}}c_s p^2$ where $\sigma_0 = \rho\sqrt{c_{22}}c_s v_0$ and $\sqrt{c_{22}}c_s$ is the dilatational wave speed when wave propagation is parallel to the y-axis. Therefore

$$K_I^*(p) = \sigma_0 \sqrt{\frac{2c_s\xi}{\sqrt{c_{22}}}} \frac{1}{p^{3/2}}, \tag{2.67}$$

and by Laplace transform inversion the dynamic stress intensity factor in the time domain for the semi-infinite punch problem may be found. This is

$$K_I(t) = 2\sigma_0 \sqrt{\frac{2c_s\xi}{\pi\sqrt{c_{22}}}} \sqrt{t}. \tag{2.68}$$

Note that (2.68) is the same as that for the case of the semi-infinite crack problem subject to uniform impact loading on the crack faces in mode I, that result has been reported by Rubio-Gonzalez and Mason [12].

25

2.3 Finite Punch

2.3.1 Method of solution

For a finite-width punch $(0 < x < 2l)$ a solution can be obtained by superposition of solutions for semi-infinite punches. Due to the fact that any disturbance propagates at a finite speed, the solution for a semi-infinite punch is valid as long as diffraction waves from an opposite edge have not arrived at the region under consideration.

Consider a rigid punch of length $2l$ acting on a half plane $y \geq 0$ with $v(x, 0, t) = f_0(t)$ (figure 2.3), the boundary $y = 0$ outside the punch is stress free. The punch is symmetrical, therefore the solution to be found is symmetrical with respect to the straight line $x = l$, *i.e.*

$$v(2l - x, y, t) = v(x, y, t), \qquad \sigma_y(2l - x, y, t) = \sigma_y(x, y, t). \tag{2.69}$$

Hence it is sufficient to find the solution in the region $\{x \leq l, \ y \geq 0\}$.

First consider the problem for $0 < t < l/c_d$. Throughout this interval the diffraction disturbances M_0 and N_0 from opposite edges of the punch $(x = 0, \ x = 2l)$ do not interact, see figure 2.3(a), so the solution at $x \leq l$ will be the same as in the problem on penetration by a semi-infinite punch $(0 < x < \infty)$. Then the stress under the punch $(0 < x < 2l)$ for $0 < t < l/c_d$ may be written as

$$\sigma_y(x, 0, t) = -\rho\sqrt{c_{22}}c_s f_0'(t) + \sigma_y^{(0)}(x, 0, t) + \sigma_y^{(0)}(2l - x, 0, t), \tag{2.70}$$

where $\sigma_y^{(0)}(x, 0, t)$ is the solution for a semi-infinite punch $(0 < x < \infty)$ and $-\rho\sqrt{c_{22}}c_s f_0'(t)$ being the solution to the one-dimensional problem on indentation by an infinite punch $(-\infty < x < \infty)$. Recall that $\sqrt{c_{22}}c_s$ is the dilatational wave speed for wave propagation parallel to the y-axis.

For $l/c_d < t < 2l/c_d$, figure 2.3(b), it follows from the linearity of the problem that the stress under the punch is a result of superimposing the disturbances $\sigma_y^{(0)}(x, 0, t)$ and $\sigma_y^{(0)}(2l - x, 0, t)$ propagating from the left and right edges, respectively, so, equation (2.70) remains valid throughout this time interval.
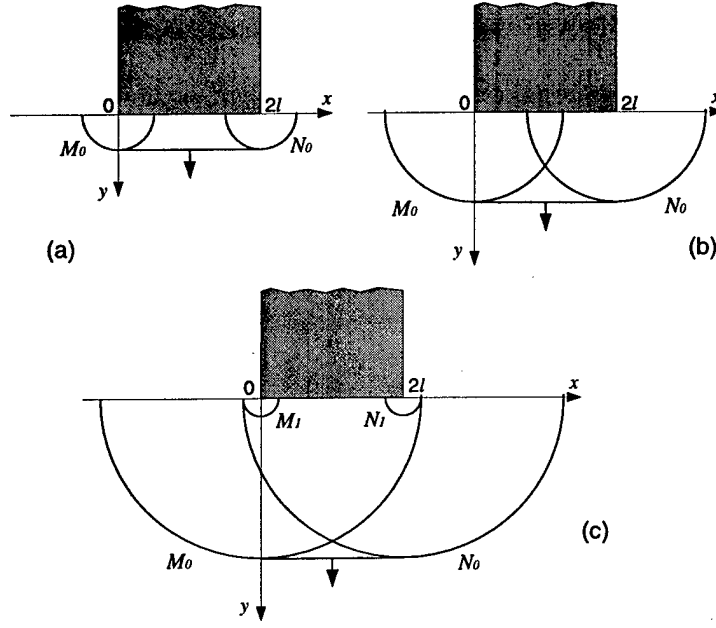
Figure 2.3: Schematic representation of the propagation of disturbances for (a) $0 < t < l/c_d$, (b) $l/c_d < t < 2l/c_d$, (c) $2l/c_d < t < 3l/c_d$.

For $2l/c_d < t < 3l/c_d$, a new pair of diffraction waves M_1 and N_1 occurs, figure 2.3(c). These new disturbances must behave outside the punch so as to nullify the disturbances M_0 and N_0 which come from opposite edges and violate the boundary conditions on $y = 0$ outside the punch.

For $2l/c_d < t < 3l/c_d$ when these disturbances do not interact, supplementary distur-bances $\sigma_y^{(1)}$ and $v^{(1)}$ within the domain $x \leq l$ (which are caused by the appearance of the diffraction wave M_1 near the left edge at $t_1 > 0$, $t_1 = t - 2l/c_d$) are governed by the following boundary conditions on the axis $y = 0$:

$$\sigma_y^{(1)}(x, 0, t_1) = -\sigma_y^{(0)}(2l - x, 0, t_1) \quad x < 0, \tag{2.71}$$

$$v^{(1)}(x, 0, t_1) = 0 \quad x > 0. \tag{2.72}$$

At $3l/c_d < t < 4l/c_d$, disturbances in the stress under the punch are a result of superpo-sition of the disturbances $\sigma_y^{(1)}(x, 0, t_1)$ and $\sigma_y^{(1)}(2l - x, 0, t_1)$ caused by the diffraction waves M_1 and N_1 symmetrical with respect to the line $x = l$. The same is valid over a wider range $2l/c_d \leq t < 4l/c_d$.

27

Thus once t exceeds $2ln/c_d$ ($n = 1, 2, 3, \ldots$), there appears a new (nth) pair of diffraction waves, M_n and N_n. They carry supplementary disturbances symmetrical with respect to the line $x = l$ with boundary conditions

$$\sigma_y^{(n)}(x, 0, t_n) = -\sigma_y^{(n-1)}(2l - x, 0, t_n) \quad x < 0, \tag{2.73}$$

$$v^{(n)}(x, 0, t_n) = 0 \quad x > 0, \tag{2.74}$$

with zero initial conditions at $t_n = 0$, where $t_n = t - 2nl/c_d \geq 0$.

Solution to the problem with boundary conditions (2.73) and (2.74) is the same as in the case of a semi-infinite punch with boundary conditions (2.8) after changing t, $\sigma_-(x, t)$, $f_0(x, t)$, $\sigma_y(x, 0, t)$ and $v(x, 0, t)$ by t_n, $-\sigma_y^{(n-1)}(2l - x, 0, t_n)$, 0, $\sigma_y^{(n)}(x, 0, t_n)$, and $v^{(n)}(x, 0, t_n)$ respectively. As a result, the stress under the punch $0 < x < 2l$ at $2kl/c_d \leq t < 2l(k+1)/c_d$ ($k = 0, 1, 2, \ldots$) is

$$\sigma_y(x, 0, t) = -\rho\sqrt{c_{22}}c_s f_0'(t) + \sum_{n=0}^{k} \left[\sigma_y^{(n)}(x, 0, t_n) + \sigma_y^{(n)}(2l - x, 0, t_n) \right], \tag{2.75}$$

where $t_n = t - 2nl/c_d$.

2.3.2   Stress intensity factor

An expression for the dynamic stress intensity factor near the punch corners valid for $0 < t < 4l/c_d$ will be developed in this subsection. From equation (2.75) with $k = 1$ we may write

$$K_I(t) = \begin{cases} K_I^{(0)}(t) & \text{for} \quad 0 < t < 2l/c_d \\ K_I^{(0)}(t) + K_I^{(1)}(t) & \text{for} \quad 2l/c_d < t < 4l/c_d \end{cases} \tag{2.76}$$

where $K_I^{(0)}(t)$ and $K_I^{(1)}(t)$ may be called contributions of zero and first orders respectively. $K_I^{(0)}(t)$ corresponds to the stress intensity factor for the semi-infinite punch, equation (2.68), this is associated with $\sigma_y^{(0)}(x, 0, t)$. That is

$$K_I^{(0)}(t) = 2\sigma_0\sqrt{\frac{2c_s\xi}{\pi\sqrt{c_{22}}}} \sqrt{t}. \tag{2.77}$$

On the other hand, $K_I^{(1)}(t)$ takes into account the effect of the appearance of the first diffraction wave M_1, so $K_I^{(1)}(t)$ is associated with $\sigma_y^{(1)}(x, 0, t)$.

28

According to (2.71) and (2.72)

$$\Sigma_-^{(1)}(s) = -e^{2sli}\Sigma_+^{(0)}(-s), \tag{2.78}$$

$$V_+^{(1)}(s) = 0. \tag{2.79}$$

To find the stress intensity factor $K_I^{(1)}(t)$, an asymptotic expression of $\Sigma_+^{(1)}(s)$ as $s \to \infty$ is required. First note that $\Sigma_+^{(0)}(s)$ for the semi-infinite punch is given by (2.63), then using $\hat{F}_+(-s) = \hat{F}_-(s)$, equation (2.78) becomes

$$\Sigma_-^{(1)}(s) = -e^{2sli}\frac{(-s + ip/c_R)}{\sqrt{-s + ip/c_d}}L_-(0)f_0^*(p)\frac{\hat{F}_-(s)}{is}. \tag{2.80}$$

From (2.56), (2.55) and (2.47) with $V_+(s) = 0$ and $\Sigma_-(s)$ given by (2.80) it possible to show that

$$D_+(s,p) = -\frac{L_-(0)f_0^*(p)}{i}\frac{1}{2\pi i}\int_{-\infty+i\lambda_0}^{\infty+i\lambda_0}\frac{(-z + ip/c_R)\sqrt{z + ip/c_d}}{(z + ip/c_R)\sqrt{-z + ip/c_d}}\frac{\hat{F}_-(z)}{z\hat{F}_+(z)}e^{2zli}\frac{dz}{z-s}, \tag{2.81}$$

inserting this expression into (2.58), the desired asymptotic expression is obtained as

$$\Sigma_+^{(1)}(s) = -\frac{\mu_{12}\xi}{\sqrt{-i}\sqrt{s}}\frac{\sqrt{c_d}}{c_R}\sqrt{p}f_0^*(p)\hat{F}_-(0)\frac{1}{2\pi i}\int_{-\infty+i\lambda_0}^{\infty+i\lambda_0}\frac{(-z + ip/c_R)\sqrt{z + ip/c_d}}{(z + ip/c_R)\sqrt{-z + ip/c_d}}$$

$$\frac{\hat{F}_-(z)}{z\hat{F}_+(z)}e^{2zli}dz \quad \text{as} \quad s \to \infty \tag{2.82}$$

where equation (2.64) for $L_-(0)$ has been used. Making the change of variable $z = ip\zeta$ and using (2.62), the stress intensity factor in the Laplace transform domain may be written as

$$K_I^{*(1)}(p) = -\sqrt{2}\mu_{12}\xi\frac{\sqrt{c_d}}{c_R}\sqrt{p}f_0^*(p)\hat{F}_-(0)\frac{1}{2\pi i}\int_{\tau_0-i\infty}^{\tau_0+i\infty}I(\zeta)e^{-2p\zeta l}d\zeta \tag{2.83}$$

where

$$I(\zeta) = \frac{(-\zeta + 1/c_R)\sqrt{\zeta + 1/c_d}}{(\zeta + 1/c_R)\sqrt{-\zeta + 1/c_d}}\frac{\tilde{F}_-(\zeta)}{\zeta\tilde{F}_+(\zeta)}. \tag{2.84}$$

To perform the inversion of $K_I^*(p)$ the Cagniard-de Hoop method can be applied. The central idea of the Cagniard-de Hoop scheme [20, 16] is to convert the integral in (2.83) to a form which allow inversion of the one-sided Laplace transform *by observation*. The path of

integration is modified to form a closed contour, figure 2.4, such that the integrand in (2.83) is analytic inside of this contour. Consider again the case where the punch approaches the orthotropic half-plane with constant velocity v_0, then $f_0^*(p) = v_0/p^2 = \sigma_0/\rho\sqrt{c_{22}}c_s p^2$. Applying Cauchy's theorem, Jordan's lemma and the fact that $I(\bar{\zeta}) = \overline{I(\zeta)}$ one can write $K_I^{*(1)}(p)$ as

$$K_I^{*(1)}(p) = -\sqrt{2}\mu_{12}\xi\frac{\sqrt{c_d}}{c_R}\frac{\sigma_0}{\rho\sqrt{c_{22}}c_s\pi}\hat{F}_-(0)\frac{1}{p^{3/2}}\int_{1/c_d}^{\infty}\text{Im}[I(\zeta)]e^{-2p\zeta l}d\zeta. \qquad (2.85)$$

Letting $2\zeta l = \eta$, this equation becomes

$$K_I^{*(1)}(p) = -\sqrt{2}\mu_{12}\xi\frac{\sqrt{c_d}}{c_R}\frac{\sigma_0}{\rho\sqrt{c_{22}}c_s\pi 2l}\hat{F}_-(0)\frac{1}{p^{3/2}}\int_0^{\infty}\text{Im}[I(\eta/2l)]e^{-\eta p}H(\eta - 2l/c_d)d\eta. \qquad (2.86)$$

and the inversion of the Laplace transform becomes obvious. Equation (2.86) is a product of two transforms, so that $K_I^{(1)}(t)$ is a convolution of the inverse of the two transforms, *i.e.*

$$K_I^{(1)}(t) = -4\sigma_0\xi\frac{\sqrt{c_d}c_s}{c_R\sqrt{c_{22}}}\frac{1}{\pi}\sqrt{\frac{l}{\pi}}\hat{F}_-(0)\int_{1/c_d}^{\hat{t}}\text{Im}[I(\eta)]\sqrt{\hat{t}-\eta}\,d\eta, \qquad (2.87)$$

and, by substitution of $\hat{F}_-(0)$ yields

$$K_I^{(1)}(t) = -4\sigma_0\frac{\sqrt{\pi l}}{\pi^2}\sqrt{\frac{\xi c_s}{\sqrt{c_{22}}}}\int_{1/c_d}^{\hat{t}}\text{Im}[I(\eta)]\sqrt{\hat{t}-\eta}\,d\eta. \qquad (2.88)$$
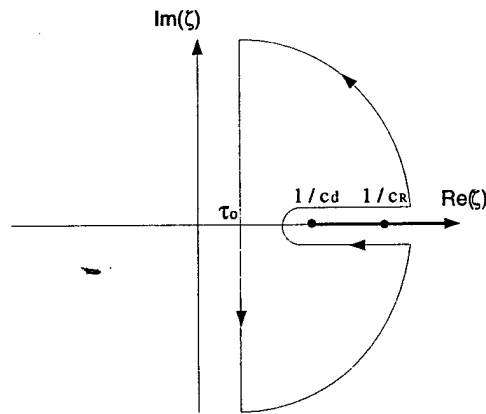
where $\hat{t} = t/2l$.

Figure 2.4: Contour of integration to evaluate the integral in (2.83) in the $\zeta-$ plane.

30

2.4 Semi-infinite Crack

The semi-infinite crack problem is considered in this section. The analysis follows that of the punch case with some minor differences. So there is no need to repeat the analysis of the last sections and only the important points will be outlined.

2.4.1 Method of Solution

Consider the plane problem of an infinite orthotropic medium containing a semi-infinite crack, figure 2.5. The crack faces are along the negative $x-$axis and the origin of the xy coordinate system is in the crack tip. Let $\sigma_-(x,t)$ be the pressure applied on the crack faces, and consider a more general problem where the displacement ahead of the crack tip is given by $f_0(x,t)$, thus the boundary conditions are

$$
\begin{aligned}
\sigma_y(x,0,t) &= \sigma_-(x,t) \quad &\text{for} \quad -\infty < x < 0, \\
\tau_{xy}(x,0,t) &= 0 \quad &\text{for} \quad -\infty < x < \infty, \\
v(x,0,t) &= f_0(x,t) \quad &\text{for} \quad x \geq 0.
\end{aligned}
\tag{2.89}
$$

In addition, the condition of zero displacements at infinity and zero initial conditions are assumed. Note that with $f_0(x,t) \equiv 0$ the standard problem with the semi-infinite crack is recovered [12]. The function $f_0(x,t)$ is assumed to be zero at any $x > c_d t + k$, $(k \geq 0)$.
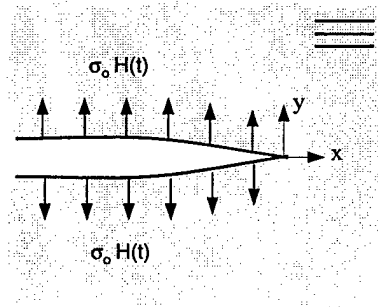

Figure 2.5: Schematic of the semi-infinite crack geometry.

The differential equations describing this problem are (2.1) and (2.2) with boundary conditions (2.89). Therefore the same procedure as for the punch problem is applied, i.e.,

31

application of Laplace and Fourier transforms to the equations of motion and boundary conditions following by the use of the Wiener-Hopf technique to find $\Sigma_+(s)$ and $V_-(s)$ which are given by (2.58) and (2.59). It should be noted that in this case, the planes of analyticity of the double transforms $\Sigma_+(s)$ and $V_-(s)$ will be $\text{Im}(s) > -p/c_d$ and $\text{Im}(s) < 0$ respectively.

For the standard semi-infinite crack problem $f_0(x,t) \equiv 0$ and $\sigma_-(x,t) = -\sigma_0 H(t)$, hence $V_+(s) = 0$ and $\Sigma_-(s) = -\sigma_0/ips$. Therefore (2.47) reduces to $D(s) = -L_+(s)\sigma_0/ips$ and its factorization follows easily

$$D(s) = -\frac{\sigma_0}{ips}L_+(s) = -\frac{\sigma_0}{p}\left[\frac{L_+(s) - L_+(0)}{is} + \frac{L_+(0)}{is}\right], \tag{2.90}$$

$$D_-(s) = -\frac{\sigma_0}{p}\frac{L_+(0)}{is}, \tag{2.91}$$

and hence the unknown functions $\Sigma_+(s)$ and $V_-(s)$ are

$$\Sigma_+(s) = \frac{(s + ip/c_R)}{\sqrt{s + ip/c_d}}\frac{\sigma_0}{p}\left[\frac{L_+(s) - L_+(0)}{is}\right]\hat{F}_+(s), \tag{2.92}$$

$$V_-(s) = \frac{\sqrt{s - ip/c_R}}{\mu_{12}\xi(s - ip/c_d)}\frac{\sigma_0}{p}\frac{L_+(0)}{is}\frac{1}{\hat{F}_+(s)}. \tag{2.93}$$

Following the same procedure as in the semi-infinite, smooth, rigid punch problem we can get the stress intensity factor for the standard semi-infinite crack problem with uniform impact pressure on the crack faces, this is

$$K_I(t) = 2\sigma_0\sqrt{\frac{2c_s\xi}{\pi\sqrt{c_{22}}}}\sqrt{t}. \tag{2.94}$$

2.5 Finite Crack

2.5.1 Method of Solution

A solution for the finite crack problem will be obtained by superposition of solutions for semi-infinite cracks. Consider an infinite orthotropic plate containing a crack of length $2l$ with crack faces parallel to the x–axis and the crack tips located at $x = -2l$ and $x = 0$, figure 2.6. By symmetry it is expected that the solution is symmetric with respect to the

line $x = -l$, that is

$$v(-2l - x, y, t) = v(x, y, t), \qquad \sigma_y(-2l - x, y, t) = \sigma_y(x, y, t). \tag{2.95}$$

Hence it is sufficient to find the solution in the region $\{x \geq -l, \ y \geq 0\}$.

For the time interval $0 < t < 2l/c_d$, the stress field is

$$\sigma_y(x, 0, t) = -\sigma_0 + \sigma_y^{(0)}(x, 0, t) + \sigma_y^{(0)}(-2l - x, 0, t), \tag{2.96}$$

where $\sigma_y^{(0)}(x, 0, t)$ is the solution for a semi-infinite crack.

For $2l/c_d < t < 4l/c_d$, supplementary disturbances $\sigma_y^{(1)}$ and $v^{(1)}$ within the domain $x \geq -l$ (which are caused by the appearance of the diffraction wave N_1 near the right tip at $t_1 > 0, \ t_1 = t - 2l/c_d$) are governed by the following boundary conditions on the axis $y = 0$:

$$\sigma_y^{(1)}(x, 0, t_1) \ = \ 0 \qquad x < 0, \tag{2.97}$$

$$v^{(1)}(x, 0, t_1) \ = \ -v^{(0)}(-2l - x, 0, t_1) \qquad x > 0. \tag{2.98}$$

Note that the boundary condition (2.98) is just to nullify the disturbances that come from opposite crack tips and violate the boundary conditions on $y = 0$ outside the crack.
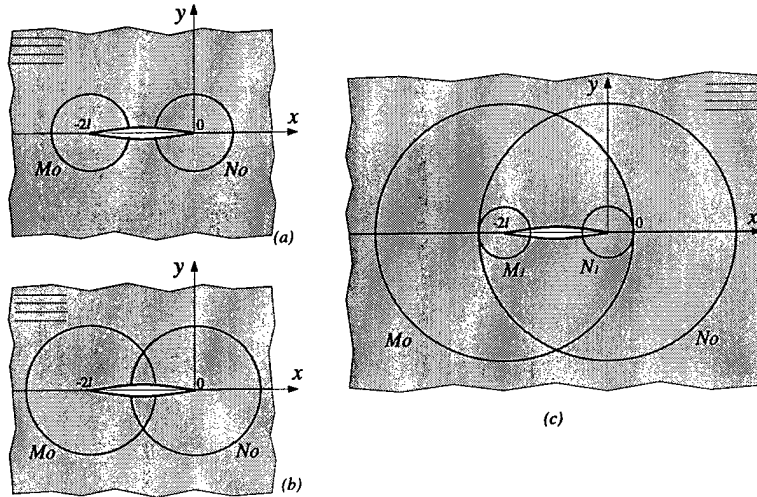

Figure 2.6: Schematic representation of the propagation of disturbances for (a) $0 < t < l/c_d$, (b) $l/c_d < t < 2l/c_d$, (c) $2l/c_d < t < 3l/c_d$.

Thus once t exceeds $2ln/c_d$ ($n = 1, 2, 3, \ldots$), there appears a new (nth) pair of diffraction waves, M_n and N_n. They carry supplementary disturbances symmetrical with respect to the

line $x = -l$ with boundary conditions

$$\sigma_y^{(n)}(x, 0, t_n) \;=\; 0 \qquad x < 0, \tag{2.99}$$

$$v^{(n)}(x, 0, t_n) \;=\; -v^{(n-1)}(-2l - x, 0, t_n) \qquad x > 0, \tag{2.100}$$

with zero initial conditions at $t_n = 0$, where $t_n = t - 2nl/c_d \geq 0$.

Solution to the problem with boundary conditions (2.99) and (2.100) is the same as in the case of a semi-infinite crack with boundary conditions (2.89) after changing t, $\sigma_-(x,t)$, $f_0(x,t)$, $\sigma_y(x,0,t)$, and $v(x,0,t)$ by t_n, 0, $-v^{(n-1)}(-2l - x, 0, t_n)$, $\sigma_y^{(n)}(x,0,t_n)$, and $v^{(n)}(x,0,t_n)$ respectively. As a result, the stress field at $2kl/c_d \leq t < 2l(k+1)/c_d$ $(k = 0, 1, 2, \ldots)$ is

$$\sigma_y(x, 0, t) = -\sigma_0 + \sum_{n=0}^{k} \left[\sigma_y^{(n)}(x, 0, t_n) + \sigma_y^{(n)}(-2l - x, 0, t_n) \right], \tag{2.101}$$

where $t_n = t - 2nl/c_d$.

2.5.2 Stress intensity factor

An expression for the dynamic stress intensity factor near crack tips valid for $0 < t < 4l/c_d$ is developed next. From equation (2.101) with $k = 1$ we may write

$$K_I(t) = \begin{cases} K_I^{(0)}(t) & \text{for} \quad 0 < t < 2l/c_d \\ K_I^{(0)}(t) + K_I^{(1)}(t) & \text{for} \quad 2l/c_d < t < 4l/c_d \end{cases} \tag{2.102}$$

being $K_I^{(0)}(t)$ and $K_I^{(1)}(t)$ the contributions of zero and first orders respectively. $K_I^{(0)}(t)$ corresponds to the stress intensity factor for the semi-infinite crack, equation (2.94), this is associated with $\sigma_y^{(0)}(x, 0, t)$. That is

$$K_I^{(0)}(t) = 2\sigma_0 \sqrt{\frac{2c_s \xi}{\pi \sqrt{c_{22}}}} \sqrt{t}. \tag{2.103}$$

On the other hand, $K_I^{(1)}(t)$ takes into account the effect of the appearance of the first diffraction wave N_1, so $K_I^{(1)}(t)$ is associated with $\sigma_y^{(1)}(x, 0, t)$.

According to (2.97) and (2.98)

$$\Sigma_-^{(1)}(s) \;=\; 0, \tag{2.104}$$

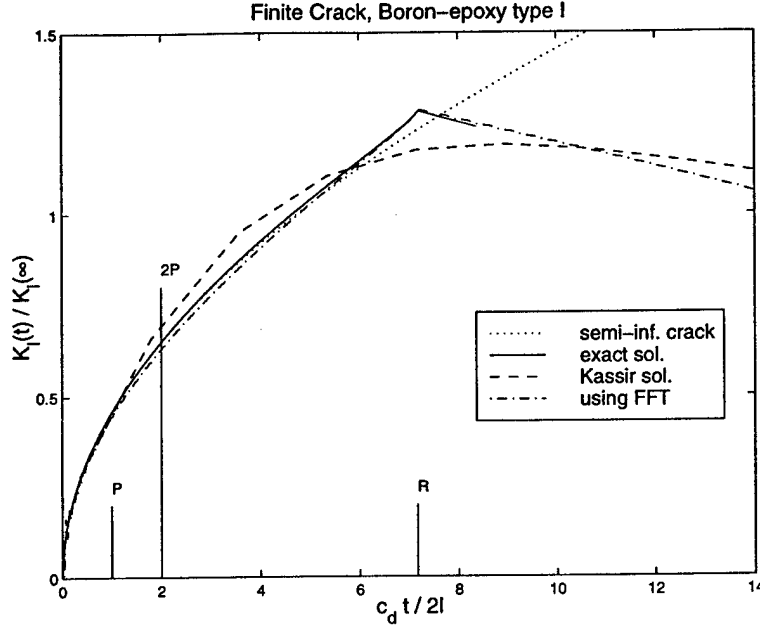$$V_+^{(1)}(s) \;=\; -e^{-2sli} V_-^{(0)}(-s). \tag{2.105}$$

34

Figure 2.7: Stress intensity factor history for a finite crack in boron-epoxy composite type I.

To find the stress intensity factor $K_I^{(1)}(t)$, an asymptotic expression of $\Sigma_+^{(1)}(s)$ as $s \to \infty$ is required. First note that $V_-^{(0)}(s)$ for the semi-infinite crack is given by (2.93), then using $\hat{F}_+(-s) = \hat{F}_-(s)$, equation (2.104) becomes

$$V_+^{(1)}(s) = e^{-2sli} \frac{\sqrt{-s - ip/c_R}}{\mu_{12}\xi(-s - ip/c_d)} \frac{\sigma_0}{p\hat{F}_+(s)} \frac{L_+(0)}{is}. \tag{2.106}$$

From (2.56), (2.55) and (2.47) with $\Sigma_-(s) = 0$ and $V_+(s)$ given by (2.106) it possible to show that

$$D_+(s,p) = \frac{\sigma_0 L_+(0)}{pi} \frac{1}{2\pi i} \int_{-\infty+i\lambda_0}^{\infty+i\lambda_0} \frac{(z - ip/c_R)\sqrt{-z - ip/c_d}}{(-z - ip/c_R)\sqrt{z - ip/c_d}} \frac{\hat{F}_-(z)}{z\hat{F}_+(z)} e^{-2zli} \frac{dz}{z - s}, \tag{2.107}$$

inserting this expression into (2.58), the desired asymptotic expression is obtained as

$$\Sigma_+^{(1)}(s) = \frac{\sigma_0 c_R}{i^{3/2}\sqrt{c_d}\hat{F}_+(0)} \frac{1}{\sqrt{s}p^{3/2}} \frac{1}{2\pi i} \int_{-\infty+i\lambda_0}^{\infty+i\lambda_0} \frac{(z - ip/c_R)\sqrt{-z - ip/c_d}}{(-z - ip/c_R)\sqrt{z - ip/c_d}}$$

$$\frac{\hat{F}_-(z)}{z\hat{F}_+(z)} e^{-2zli} dz \qquad \text{as} \quad s \to \infty \tag{2.108}$$

where $L_+(0) = c_R/\sqrt{ip}\sqrt{c_d}\hat{F}_+(0)$ has been used. Making the change of variable $z = -ip\zeta$ and using (2.62), the stress intensity factor in the Laplace transform domain may be written
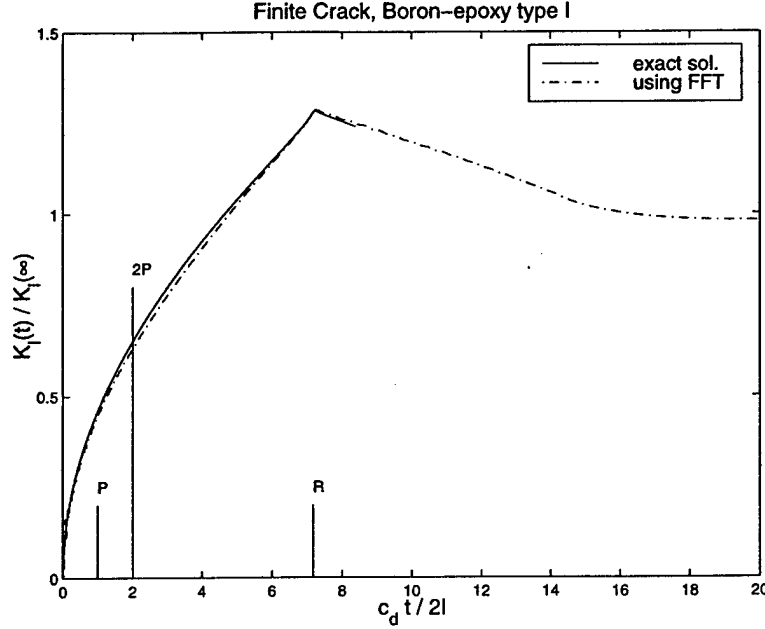
35

Figure 2.8: Comparison between the exact solution of $K_I(t)$ and the results derived using the method of Kassir (1983) but with FFT for the Laplace transform inversion, for boron-epoxy composite type I.

as

$$K_I^{*(1)}(p) = \frac{\sqrt{2}\sigma_0 c_R}{\sqrt{c_d}\hat{F}_+(0)} \frac{1}{p^{3/2}} \frac{1}{2\pi i} \int_{\tau_0-i\infty}^{\tau_0+i\infty} I(\zeta)e^{-2p\zeta l}d\zeta \qquad (2.109)$$
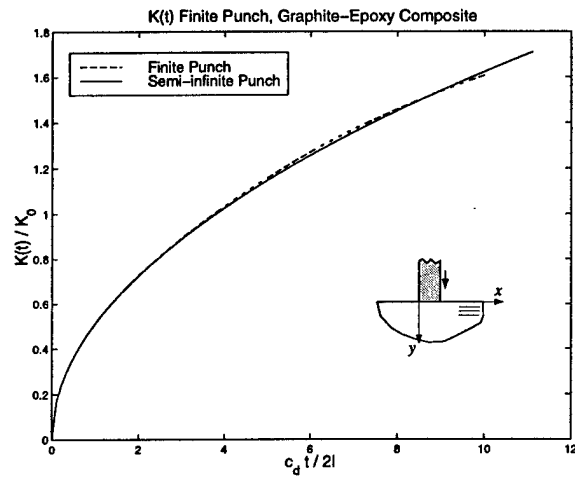
where

$$I(\zeta) = \frac{(\zeta + 1/c_R)\sqrt{-\zeta + 1/c_d}}{(-\zeta + 1/c_R)\sqrt{\zeta + 1/c_d}} \frac{\hat{F}_+(\zeta)}{\zeta\hat{F}_-(\zeta)}. \qquad (2.110)$$

To perform the inversion of $K_I^*(p)$ the Cagniard-de Hoop method can be applied as in the punch problem. After doing the inversion we get the first order contribution to the dynamic stress intensity factor in the time domain, $K_I^{(1)}(t)$, as

$$K_I^{(1)}(t) = -4\sigma_0 \frac{\sqrt{\pi l}}{\pi^2} \sqrt{\frac{\xi c_s}{\sqrt{c_{22}}}} \int_{1/c_d}^{\hat{t}} \text{Im}[I(\eta)]\sqrt{\hat{t}-\eta}\ d\eta. \qquad (2.111)$$
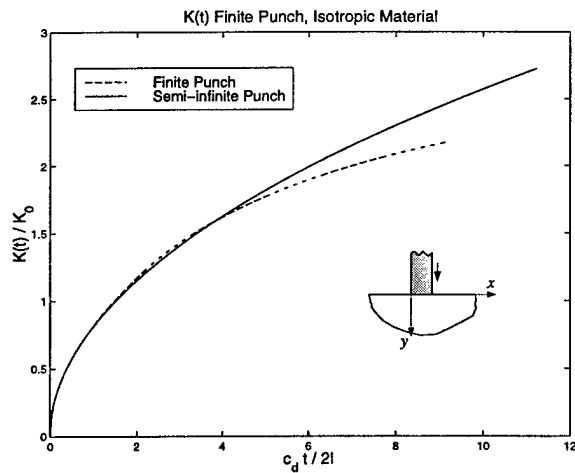
where $\hat{t} = t/2l$ and $I(\zeta)$ is given by (2.110).

36

(a)
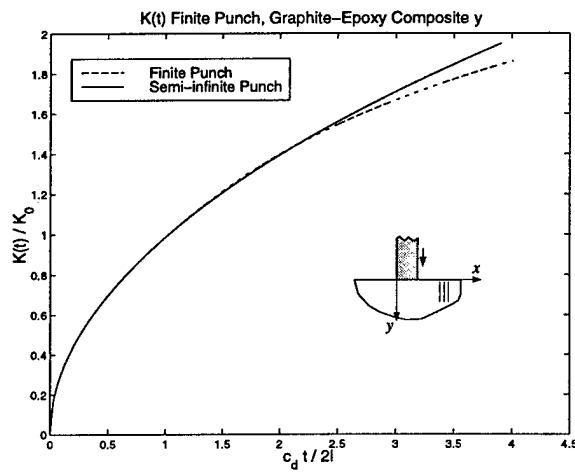
(b)

(c)

Figure 2.9: Dynamic stress intensity factor for the punch problem, (a) graphite-epoxy composite, (b) graphite-epoxy composite with fibers parallel to the y-axis, (c) isotropic material.

2.6 Results and Conclusions

2.6.1 Punch Problem

Figure 2.9 illustrates the dynamic stress intensity factor history $K_I(t)$ for the punch problem for different materials listed in Table 2.1. Note that $K_I(t)$ for the finite punch, equation (2.76), is valid only in $0 < c_d t/2l < 2$, however it has been plotted for an extended time interval to show that the first order contribution $K_I^{(1)}(t)$ is small even outside the interval of validity $0 < c_d t/2l < 2$. Figure 2.9(b) shows that for the graphite-epoxy composite with fibers parallel to the $y-$axis the stress intensity factor departs from the semi-infinite punch result at earlier normalized time than in figure 2.9(a) where the fibers are along the $x-$axis direction. The stress intensity factor is normalized with respect to $K_0 = \sigma_0 \sqrt{\pi l}$.
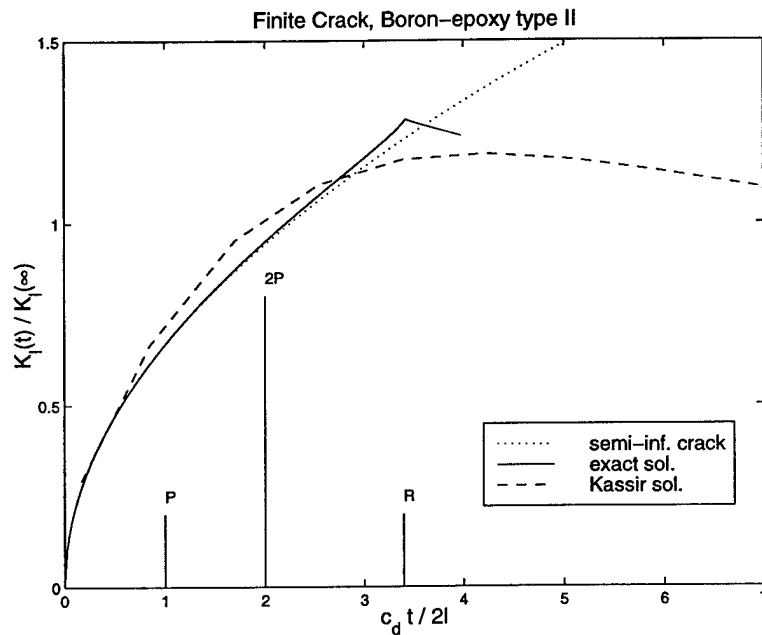

Figure 2.10: Comparison between the exact solution of $K_I(t)$ and the results derived using the method of Kassir (1983) but with FFT for the Laplace transform inversion, for boron-epoxy composite type II.

2.6.2 Crack Problem

Figures 2.7-2.11 show the dynamic stress intensity factor $K_I(t)$ for the finite crack in different materials. The labels P and R represent the arrival time of the dilatational and Rayleigh

waves respectively from the opposite crack tip. The label $2P$ means the time needed for the dilatational wave to travel the crack length twice, i.e., the solution derived here for the finite crack is valid until the time labeled with $2P$. The curved marked with "using FFT" in figures 2.7 and 2.8 represent the result obtained for $K_I(t)$ using the method of Kassir and Banyopadhyay [13], but with different numerical schemes to solve the Fredholm integral equation and using fast Fourier transform for Laplace transform inversion [21]. Comparing these results with the exact solution just developed it is concluded that such schemes were more appropriate as was claimed in [21]. The dynamic overshoot is better described. In all the cases, figures 2.7 and 2.8, the results obtained by Kassir and Banyopadhyay [13] are shown to depart from the exact solution. Figure 2.11 shows $K_I(t)$ for finite crack in graphite-epoxy composite with fibers parallel to the $y-$axis, in this case the dynamic overshoot occurs inside the time interval of validity of the exact solution, i.e., in $0 < c_d t / 2l < 2$, and hence it is accurately described. The normalization factor is the long time stress intensity factor for a finite crack, $K_I(\infty) = \sigma_0 \sqrt{\pi l}$.
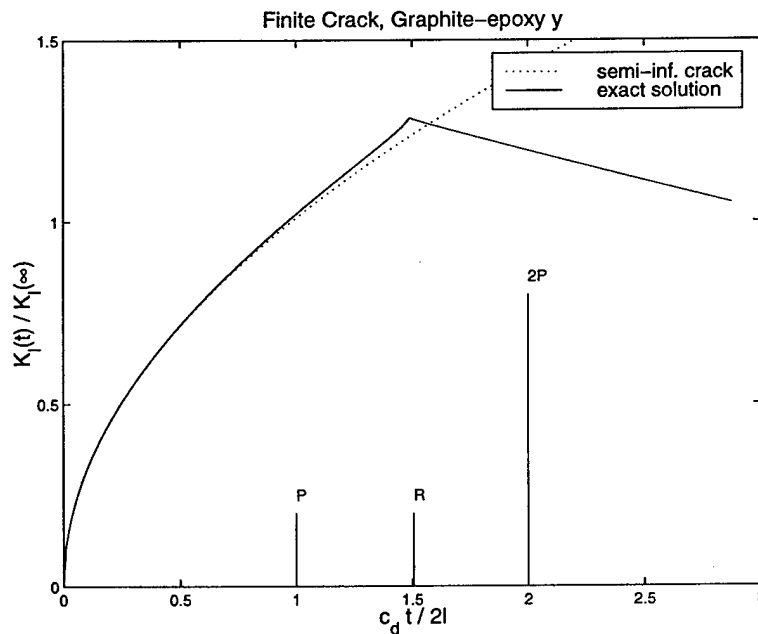

Figure 2.11: Stress intensity factor history for a finite crack in graphite-epoxy composite with fibers parallel to the $y-$axis.

	Graphite Epoxy	E-Glass Epoxy	Boron Epoxy	Epoxy
c_{11}	20.77	8.38	32.67	3.91
c_{22}	2.18	2.29	3.12	3.91
c_{12}	0.49	0.52	0.79	1.91
μ_{12} (GPa)	7.48	5.5	6.4	1.96
ρ (Kg/m^3)	1600	2100	1990	1260

Table 2.1: Mechanical properties used for the analysis.

Bibliography

[1] K. L. Johnson. *Contact Mechanics*. Cambridge University Press. New York, NY, 1987.

[2] G. M. Gladwell. *Contact Problems in the Classical Theory of Elasticity*. Sijthoff and Noordhoff. The Netherlands, 1980.

[3] L. M. Brock. Dynamic analysis of dislocation generation due to sudden indentation. *Int. J. Eng. Sci.*, 21:1437–1442, 1983.

[4] L. M. Brock. Thermal and slip mechanism effect in rapid indentation by a flat punch. *Acta Mechanica*, 114:185–201, 1996.

[5] C. Rubio-Gonzalez. *Dynamic Fracture Initiation in Composite Materials*. PhD thesis, University of Notre Dame, 1999.

[6] J. R. Willis. Self-similar problems in elastodynamics. *Phil. Trans. Royal Soc. (London)*, 274:435–491, 1973.

[7] H. G. Georgiadis and L. M. Brock. Dynamic indentation of an elastic half-plane by a rigid wedge: Frictional and tangential-displacement effects. *Int. J. Solids Structures*, 32(23):3435–3450, 1995.

[8] K. Roessig and J. Mason. Dynamic stress intensity factors in the dynamic punch test. *Eng. Fracture Mech.*, 60(4):421–435, 1998.

[9] L. B. Freund. The stress intensity factor due to normal impact loading on the faces of a crack. *Int. J. Engng. Sci.*, 12:179–189, 1974.

[10] C. Rubio-Gonzalez and J. Mason. Dynamic stress intensity factor due to concentrated normal loads on semi-infinite cracks in orthotropic materials. *Accepted in J. Composite Mat.*, 1999d.

[11] V. B. Poruchikov. *Methods of the Classical Theory of Elastodynamics*. Springer-Verlag. New York, NY, 1993.

[12] C. Rubio-Gonzalez and J. Mason. Dynamic stress intensity factors at the tip of a uniformly loaded semi-infinite crack in an orthotropic material. *Accepted in J. Mech. Phys. Solids*, 1999c.

[13] M. K. Kassir and K. K. Bandyopadhyay. Impact response of a cracked orthotropic medium. *ASME, J. Appl. Mech.*, 50:630–636, 1983.

[14] E. P. Chen and G. C. Sih. Transient response of cracks to impact loads. In G.C. Sih, editor, *Elastodynamic Crack problems*, pages 1–58. Noordhoff International Publishing, 1977.

[15] S. A. Thau and T. H. Lu. Transient stress intensity factors for a finite crack in an elastic solid caused by a dilatational wave. *Int. J. Solids Structures*, 7:731–750, 1971.

[16] L. B. Freund. *Dynamic Fracture Mechanics*. Cambridge University Press. New York, NY, 1990.

[17] A. H. Nayfeh. *Wave Propagation in Layered Anisotropic Media with Applications to Composites*. North-Holland Publishing Company. North-Holland, 1995.

[18] B. Noble. *Methods Based on the Wiener-Hopf Technique*. Pergamon. New York, NY, 1958.

[19] T. C. Ting. *Anisotropic Elasticity*. Oxford University Press. New York, NY, 1996.

[20] J. D. Achenbach. *Wave Propagation in Elastic Solid*. North-Holland Publishing Company, North-Holland, 1973.

[21] C. Rubio-Gonzalez and J. Mason. Green's functions for the stress intensity factor evolution in finite cracks in orthotropic materials. *Accepted in Int. J. of Fracture*, 1999a.

Chapter 3

Experimental Investigation of Dynamic Punch Tests on Isotropic and Composite Materials

Overview

An experimental investigation is conducted on the two-dimensional punch problem for isotropic materials and unidirectional fiber-reinforced composite materials under quasi-static and impact loading. Singular stresses are generated in the specimen near the punch corners and the stress intensity factor K_I is introduced to describe the singular stress field. Laser interferometry is used to measure in-plane stresses (transmission mode) and out-of-plane displacements (reflection mode), and then estimate the stress intensity factor. In the dynamic case, a high speed photography technique was employed to capture the transient response of the specimen and measure $K(t)$ just after the impact. In all the cases a good agreement between the measurements of K and the theoretical predictions was found.

3.1   Introduction

The potential use of composite materials in the construction of defense structures makes it necessary to understand the initiation of damage in the composite as caused by impacting fragments. Typically, this kind of damage initiation is simulated in the laboratory by the punch test. In such a test, fiber-reinforced epoxy matrix composites will develop a limited amount of plasticity before failure occurs. This fact suggests an elastic solution of the stress field will play an important role in understanding and predicting the behavior of composites under punch test, impact conditions.

Like in fracture mechanics, a stress intensity factor K_I is introduced in this work to characterize the behavior of the singular stresses around the punch corners. This parameter is measured experimentally using laser interferometry and then compared with theoretical predictions. The experimental investigation is conducted on the quasi-static and dynamic punch test for isotropic and orthotropic materials. In the test, a rigid punch comes in contact with one side of the specimen, figure 3.1. The lateral shearing interferometer of coherent gradient sensing (CGS), in conjunction with high speed photography, is used to obtain real

45

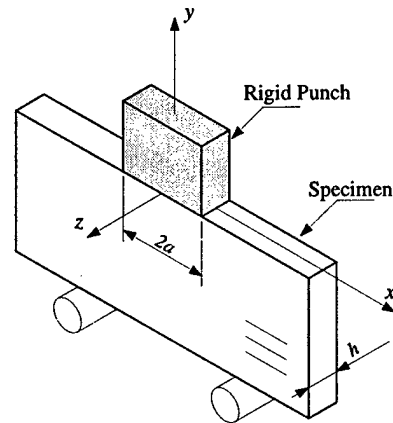time interferograms of the singular stress field generated near the corner of the punch.

Figure 3.1: Schematic of the punch test.

The application of the CGS method in the punch test is new and the verification of the dynamic solution is new as well. Here, results for isotropic as well as for composite materials are reported. In the isotropic case, the material selected was PMMA (polymethyl methacrylate) a transparent acrylic for which the CGS method in transmission mode is well suited. For the orthotropic case, the material chosen was a unidirectional graphite-epoxy composite with fiber volume fraction of 0.65.

The CGS method has been applied successfully in dynamic fracture experiments on isotropic materials [1, 2] and more recently it has been applied to dynamic fracture of fiber reinforced composite materials by Lambros and Rosakis [3, 4] and in the analysis of the quasi-static fracture behavior of composites by Liu et al. [5]. The advantage of the CGS method combined with high speed photography is that real-time visualization of dynamic fracture initiation and growth can be obtained and measurements of the dynamic stress intensity factor during these processes can be made.

The CGS method is applied to measure the stress intensity factor on the punch test on four sets of experiments; two static and two dynamic. In both cases the materials employed for the specimens are PMMA and graphite-epoxy composites. In the quasi-static test, K_I is compared successfully with known solutions of the punch problem for isotropic and orthotropic materials. In the dynamic case, each photograph taken by the high speed camera

is digitized and $K_I(t)$ is then measured. The time evolution of K_I agrees very well with the theoretical predictions for the dynamic punch problem developed in Rubio-Gonzalez and Mason [6].

3.2 Elastodynamic Analysis of the Finite Punch Problem

The punch problem is of great importance in solid mechanics for its multiple technical applications including ballistic impact, metal forming and manufacturing operations such as punching and blanking. While the quasi-static punch problem is well studied in contact mechanics [7, 8], there is little work on the dynamic case. In the dynamic case it is assumed that the punch approaches the material with a fixed velocity, and that wave propagation is involved thereby complicating the mathematical analysis.

As shown by Roessig and Mason [9] and by Rubio-Gonzalez and Mason[6] the dynamic stress intensity factor for the two-dimensional dynamic *semi-infinite* punch coincides with that for the semi-infinite crack under uniform impact loads, σ_0, applied on the crack faces in mode I. An expression for for the dynamic stress intensity factor has been developed by Rubio-Gonzalez and Mason [10], it is given by

$$K_I(t) = 2\sigma_0 \sqrt{\frac{2c_s\xi}{\pi\sqrt{c_{22}}}} \sqrt{t}, \tag{3.1}$$

where

$$\xi = \frac{\beta\sqrt{\frac{c_{22}}{c_{11}}}}{\sqrt{\beta - 2\frac{c_{12}}{c_{22}} + 2\sqrt{\frac{c_{11}}{c_{22}}}}}, \tag{3.2}$$

$$\beta = \frac{c_{11}c_{22} - c_{12}^2}{c_{22}}, \tag{3.3}$$

and $c_s = \sqrt{\mu_{12}/\rho}$ represents the velocity of the in-plane shear wave propagating along the the principal material axes and ρ is the mass density. The non-dimensional constants c_{ij} are

given by

$$c_{11} = \frac{E_1}{\mu_{12}[1 - (E_2/E_1)\nu_{12}^2]},$$
$$c_{22} = (E_2/E_1)c_{11}, \tag{3.4}$$
$$c_{12} = \nu_{12}c_{22} = \nu_{21}c_{11},$$

for generalized plane stress, and by

$$c_{11} = \frac{E_1}{\mu_{12}\Delta}(1 - \nu_{23}\nu_{32}),$$
$$c_{22} = \frac{E_2}{\mu_{12}\Delta}(1 - \nu_{13}\nu_{31}),$$
$$c_{12} = \frac{E_1}{\mu_{12}\Delta}(\nu_{21} + \frac{E_2}{E_1}\nu_{13}\nu_{32}), \tag{3.5}$$
$$\Delta = 1 - \nu_{12}\nu_{21} - \nu_{23}\nu_{32} - \nu_{31}\nu_{13} - \nu_{12}\nu_{23}\nu_{31} - \nu_{13}\nu_{21}\nu_{32},$$

for plane strain. In these equations E_i, μ_{ij} and ν_{ij} (i,j =1,2,3) are the engineering elastic constants of the material where the indices 1, 2, and 3 correspond to the directions (x, y, z) of a system of Cartesian coordinates chosen to coincide with the axes of material orthotropy.

The problem of a *finite*, rigid and flat punch impacting an orthotropic half-plane has been analyzed by Rubio-Gonzalez and Mason [6] for the orthotropic case using integral transforms and the Wiener-Hopf technique and by Roessig and Mason [9] for the isotropic case. A solution for the dynamic stress intensity factor $K_I(t)$ was developed which is valid while the dilatational wave travels the punch width twice. That is

$$K_I(t) = \begin{cases} K_I^{(0)}(t) & \text{for } 0 < t < 2l/c_d \\ K_I^{(0)}(t) + K_I^{(1)}(t) & \text{for } 2l/c_d < t < 4l/c_d \end{cases} \tag{3.6}$$

where $K_I^{(0)}(t)$ and $K_I^{(1)}(t)$ may be called contributions of zero and first orders respectively. $K_I^{(0)}(t)$ corresponds to the stress intensity factor for the semi-infinite punch, equation (3.1). On the other hand, $K_I^{(1)}(t)$ takes into account the effect of the appearance of the first diffraction wave emitted by the opposite punch corner. The velocity $c_d = \sqrt{c_{11}}c_s$ represents the dilatational wave speed along the x−axis.

It was found that $K_I^{(1)}(t)$ makes a small contribution to $K_I(t)$ in equation (3.6). Thus, for the dynamic punch test, the experimental results will be compared to $K_I^{(0)}(t)$ given by equation (3.1).

It has been shown [10] that the orthotropic formulation includes the isotropic result as special case. That is, $K_I(t)$ for isotropic materials is recovered from the orthotropic expression (3.1) with the proper substitution of the elastic constants and it is given by

$$K_I(t) = 2\sigma_0 \frac{\sqrt{c_d(1-2\nu)/\pi}}{(1-\nu)}\sqrt{t}. \tag{3.7}$$

This expression was developed for the isotropic case by Freund. [11]

Note that in both cases, equations (3.1) and (3.7), the stress intensity factor is proportional to the square root of time and may be written in the form

$$K_I(t) = \sigma_0 C_I \sqrt{t},$$

where the material-related constant C_I is

$$C_I = 2\sqrt{\frac{2c_s\xi}{\pi\sqrt{c_{22}}}}, \tag{3.8}$$

for the orthotropic case, and

$$C_I = 4\frac{c_s}{c_d}\sqrt{c_d(1-c_s^2/c_d^2)/\pi}, \tag{3.9}$$

for the isotropic case.

Equations (3.1) and (3.7) were derived under the assumption that the semi-infinite crack face loading (or semi-infinite punch) was suddenly applied. Once $K_I(t)$ is established for the step loading, the corresponding result for any time loading may be obtained by superposition [11]. For the particular case of a step load of finite duration t^*, the resulting stress intensity factor is given by

$$K_I(t) = \sigma_0 C_I \left[\sqrt{t}H(t) - \sqrt{t-t^*}H(t-t^*)\right], \tag{3.10}$$

where C_I is given by equations (3.8) and (3.9) for the orthotropy and isotropic cases, respectively.

3.3 Coherent Gradient Sensing (CGS)

CGS is a full field optical method that may be used to study deformations in transparent as well as opaque solids. This technique provides measures of either in-plane gradients of stresses (transmission) or in-plane gradients of out-of-plane displacements (reflection). Consider a specimen of uniform thickness in the undeformed state with the mid-plane coinciding with the $x - y$ plane, see figure 3.2. The specimen is loaded so that it causes nonuniform spatial gradients in the optical path when light is transmitted through it or reflected from its surface. These gradients are related to the deformation. For transmission of light through a transparent specimen gradients in refractive index are related to gradients of stress through the stress-optic coefficient, for reflection, gradients in nonuniform out-of-plane displacements are related to deformation through the Poisson effect.

Experimental Arrangement

The schematic of the experimental setup used for transmission CGS is shown in figure 3.2(a). A transparent optically isotropic plate specimen is illuminated by a collimated beam of coherent laser light. The transmitted wave passes through a pair of high density gratings G_1 and G_2, separated by a distance Δ. The field distribution on the G_2 plane is spatially transformed by the lens L_1. By locating a filtering aperture around either the ± 1 diffraction orders at the filter plane, information regarding the stress gradients is obtained on the image plane of the lens L_2.

Figure 3.2(b) shows the modification of the above setup for measuring surface deflection of opaque solids when studied in reflection mode. In this case, the specularly reflecting specimen surface is illuminated by a collimated beam of laser light. The reflected beam, as in the previous case, is processed through the optical arrangement which is identical to the one shown in figure 3.2(a).

A brief discussion of the analysis of the system as described by Mason et al. [12] now follows. After exiting from the deformed specimen, the beam falls upon the first of two
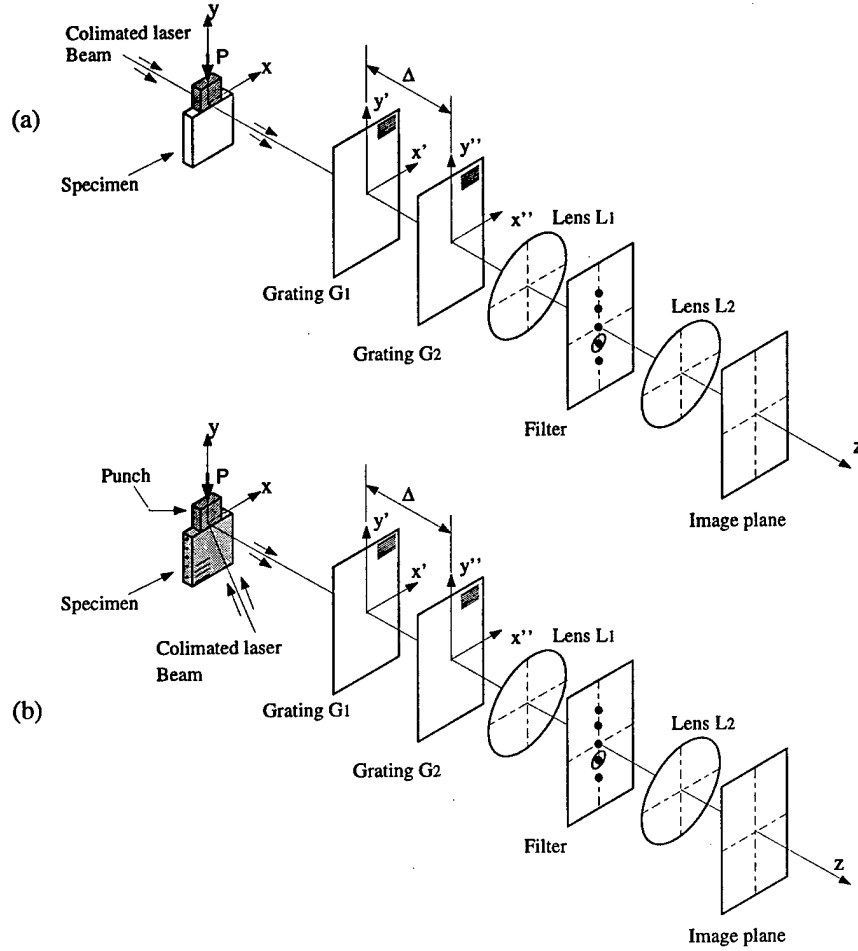
50

Figure 3.2: Schematic of the experimental setup for (a) transmission CGS, and (b) reflection CGS.

identical diffraction gratings, see figure 3.3. The primary grating G_1 splits the beam into a direct beam and numerous diffraction orders. For the sake of brevity only the first diffraction orders (± 1) and the direct beam are considered. The second diffraction grating diffracts both the direct beam and the first diffraction orders into three beams each, giving a total of nine beams behind the second grating. Of these nine beams the $(0, \pm 1)$ and $(\pm 1, 0)$ are parallel. A filtering lens can then be used to focus these parallel beams to a single spot. In the focal plane, a spatial filter is used to eliminate all superfluous beams. Another lens is then required to produce the final image.

The wave that impinges on the first diffraction grating G_1 is assumed to be parallel with some phase difference, $S(x, y)$, due to the deformations in the specimen. The two gratings
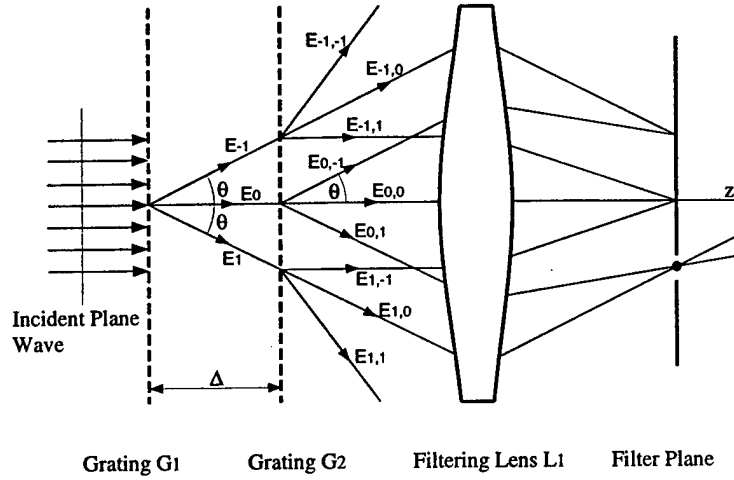
Figure 3.3: Schematic of the principle of CGS.

shift one beam with respect to the other by a distance

$$\epsilon = \Delta \tan \theta \approx \Delta \theta, \tag{3.11}$$

where Δ is the separation between the gratings and θ is the angle of diffraction as shown in figure 3.3. The diffraction angle is given by the relation

$$\theta = \sin^{-1} \frac{\lambda}{p} \approx \frac{\lambda}{p}, \tag{3.12}$$

where λ is the wavelength of the light and p is the grating pitch.

The two parallel, sheared wavefronts constructively interfere if their phase difference is an integer multiple of the wavelength, or

$$S(x + \epsilon, y) - S(x, y) = m\lambda. \tag{3.13}$$

Dividing by ϵ yields

$$\frac{S(x + \epsilon, y) - S(x, y)}{\epsilon} = \frac{m\lambda}{\epsilon}, \tag{3.14}$$

which, for small ϵ, can be approximated as

$$\frac{\partial [S(x, y)]}{\partial x} = \frac{mp}{\Delta}. \tag{3.15}$$

Equation (3.15) is valid for the derivative in either the x or y directions.

For a transparent materials, the phase difference $S(x,y)$ is composed by two contributions; the changes in specimen thickness due to Poisson's contraction, and the change in refractive index of the material due to variations in hydrostatic stress (Maxwell relation). It is possible to show [1] that for an isotropic and linearly elastic material under plane stress conditions, $S(x,y)$ is given by

$$S(x,y) \approx ch(\sigma_x + \sigma_y), \qquad (3.16)$$

where c is a modified stress-optic constant, h is the thickness and σ_x and σ_y are plane stress thickness averages of the stress components in the material. Substituting (3.16) into (3.15) gives the result

$$ch\frac{\partial(\sigma_x + \sigma_y)}{\partial x} = \frac{mp}{\Delta}, \qquad m = 0, \pm 1, \pm 2, \ldots \qquad (3.17)$$

For an opaque material reflecting the incident laser light, the phase difference, $S(x,y)$, is wholly attributed to changes in specimen thickness due to lateral contraction, thus

$$S(x,y) = 2w, \qquad (3.18)$$

where w is the $z-$component of the displacement vector. Substituting (3.18) into (3.15) yields

$$\frac{\partial w}{\partial x} = \frac{mp}{2\Delta}, \qquad m = 0, \pm 1, \pm 2, \ldots \qquad (3.19)$$

Summarizing, the formation of constructive interference on the image plane is governed by

transmission

$$ch\frac{\partial(\sigma_x + \sigma_y)}{\partial x} = \frac{mp}{\Delta}, \qquad m = 0, \pm 1, \pm 2, \ldots \qquad (3.20)$$

$$ch\frac{\partial(\sigma_x + \sigma_y)}{\partial y} = \frac{np}{\Delta}, \qquad n = 0, \pm 1, \pm 2, \ldots \qquad (3.21)$$

reflection

$$\frac{\partial w}{\partial x} = \frac{mp}{2\Delta}, \qquad m = 0, \pm 1, \pm 2, \ldots \qquad (3.22)$$

$$\frac{\partial w}{\partial x} = \frac{np}{2\Delta}, \qquad n = 0, \pm 1, \pm 2, \ldots \qquad (3.23)$$

where h is the nominal thickness of the specimen, p the grating pitch, Δ the separation between gratings and c the modified stress-optic constant.

3.4 Preparation and Characterization of the Composite Specimens

The preparation and characterization of the specimens of PMMA demanded a minimum of work; however the preparation and characterization of composite specimens required a careful procedure in order to successfully apply the CGS technique. Details for the latter case are given below.

3.4.1 Tension Test of Composites

The graphite-epoxy composite plates used in the experiments were provided by Composite Mirror Applications Inc. of Tucson, Arizona.

First, a series of tension tests were performed to determine the material properties of this particular graphite-epoxy composite. The material was assumed to be transversely isotropic. The following properties were measured : Young's modulus E_1, E_2, Poisson's ratio ν_{12} and shear modulus μ_{12} (see figure 3.4 for definition of axes). The tension test was conducted according with recommendations of the ASTM standard D 3039M-95a *Standard Test Method for Tensile Properties of Polymer Matrix Composite Materials* and performed on screw driven machine.

Table 3.2 summarizes the material parameters for graphite-epoxy composite used in the experiments. In table 3.2 some calculated material parameters are given.

3.4.2 Specimen Preparation

As mentioned earlier, an optically flat and specularly reflecting surface is needed in order to apply the CGS technique in reflection mode. Therefore a very high quality surface preparation is required on the composite material. Due to the microstructure of the composite, it is not possible to directly deposit a reflective film on the specimen by vacuum deposition.

Table 3.1: Material properties of the particular graphite-epoxy composite used in the experiments

E_1 (GPa)	92 ±3
E_2 (GPa)	6.7 ±0.1
ν_{12}	0.38 ±0.01
μ_{12} (GPa)	3.00 ±0.05
ρ (Kg/m³)	1460 ±20

Table 3.2: Calculated material parameters of the particular graphite-epoxy composite used in the experiments. Plane stress conditions

c_{11}	30.85
c_{12}	0.85
c_{22}	2.25
μ_{12} (GPa)	3.00 ±0.05
ρ (Kg/m³)	1460 ±20
c_s (m/s)	1430 ±12
$c_{d,x}$ (m/s) parallel to the fibers	7970 ±13
$c_{d,y}$ (m/s) perpendicular to the fibers	2160 ±16
ν_{23} (m/s)	.30 ±0.01
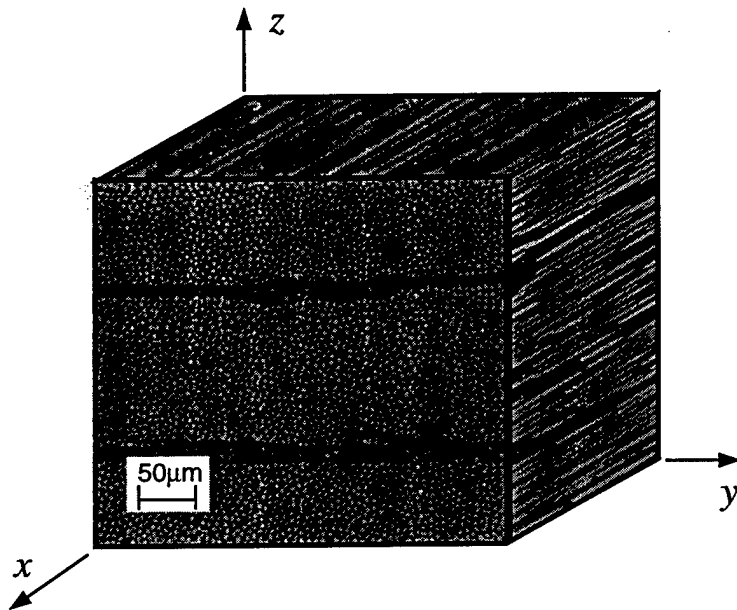
Figure 3.4: Micrographs of the unidirectional graphite-epoxy composite with fibers along the x-axis.

A procedure suggested by Liu et al.[5], with some modifications, was used to prepare the specimen surface. Figure 3.5 shows schematically the steps involved in this process. An optically flat glass is coated by vacuum deposition with a thin silver (or aluminum) film having thickness of only several angstroms. The coated glass is then combined with the sample using an epoxy adhesive to glue the coated surface of the optically flat glass to the sample. The epoxy adhesive was PC-1 Bipax of epoxy resin and diethylentrianine hardener obtained from the Photoelastic Division, Measurements Group Inc., Raleigh, N.C. After the epoxy has cured, the glass is peeled off. Because the bond between the aluminum film and the glass is weaker, the aluminum coating is transferred onto the sample surface. The total thickness of the epoxy layer and the coating is just a couple of microns. Compared with the

sample thickness, this layer is very thin and will not affect the deformation state inside the specimen.
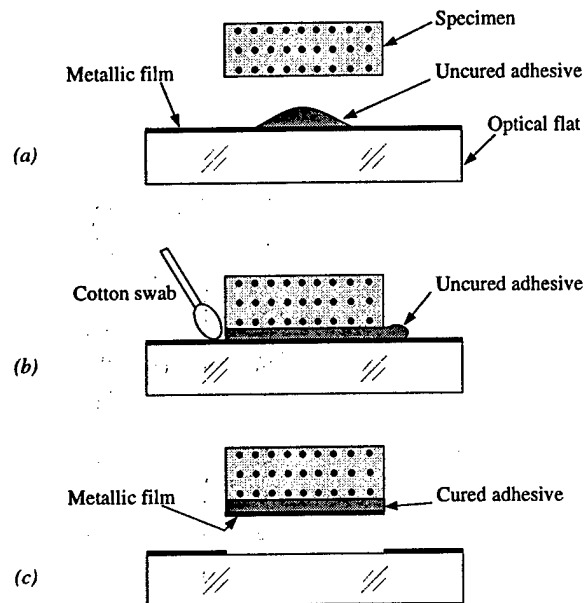
Figure 3.5: Steps involved in the composite surface preparation.

In the specimen preparation, two points are remarkably important. First, the epoxy adhesive should be free of viscoelastic effects, this guarantees the flatness of the surface minimizing the contraction during the curing time. Second, the thickness of the epoxy adhesive should be minimized to avoid shear lag effects [13], which alters the measurement of the out-of-plane deformations in regions of large strain gradients. It was found that slightly polishing the specimen surface before the application of the epoxy adhesive assists in producing a uniform epoxy layer giving better results.

3.5   Application of the CGS Method to the Quasi-Static Punch Test

First the quasi-static punch test was examined. A servohydraulic testing machine was used as a loading frame. The specimen/punch configuration is shown in figure 3.1. The materials of the specimens were PMMA and graphite-epoxy composite. Each case is analyzed separately below.

57

3.5.1 Quasi-static Punch Problem. Isotropic Material

Consider a rigid punch of length $2a$ acting on the half space as shown in figure 3.6(a). Neglecting friction, the boundary conditions for this problem are

$$\sigma_y(x,0) = 0 \quad \text{for} \quad |x| > a,$$

$$\tau_{xy}(x,0) = 0 \quad \text{for} \quad |x| < \infty, \qquad (3.24)$$

$$v(x,0) = v_0 \quad \text{for} \quad |x| < a,$$

in addition to vanishing stresses at infinity. The constant displacement of the punch, v_0, can be arbitrarily set to zero with the proper selection of the origin of the coordinates $x - y$. The total normal force applied by the punch is P.

(a)   (b)
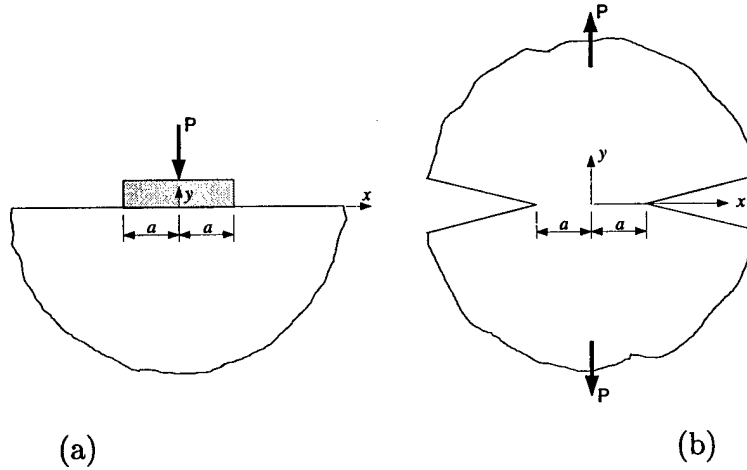
Figure 3.6: (a) Schematic of the punch problem without friction. (b) Two external semi-infinite cracks.

Note that the boundary conditions (3.24) for the rigid punch without friction are the same as for the problem of two external semi-infinite cracks, figure 3.6(b), loaded symmetrically by two remote loads P, hence both problems are described by the same mathematical solution. Using complex potentials it can be shown [14] that the stress distribution for the frictionless punch problem is given by

$$\sigma_x + \sigma_y = 2\{\phi(z) + \overline{\phi(z)}\} = 4\text{Re}\{\phi(z)\}, \qquad (3.25)$$

with

$$\phi(z) = \frac{-iP}{2\pi}\frac{1}{\sqrt{z^2 - a^2}}, \tag{3.26}$$

and $z = x + iy$. By an asymptotic analysis it can be shown that the stress field given by equations (3.25) and (3.26) is square root singular near the punch corners (or crack tips) $x = \pm a$, and a stress intensity factor can be derived as

$$K_I = \frac{P}{\sqrt{\pi a}}. \tag{3.27}$$

Taking the derivative with respect to x of equation (3.25) gives

$$\frac{\partial(\sigma_x + \sigma_y)}{\partial x} = -iK_I\sqrt{\frac{a}{\pi}}\left[\frac{z}{(z^2 - a^2)^{3/2}} - \frac{\bar{z}}{(\bar{z}^2 - a^2)^{3/2}}\right], \tag{3.28}$$

where $K_I = P/\sqrt{\pi a}$ has been used.

Now the equation governing the CGS fringes for the quasi-static punch test may be derived. For the transmission mode, combining equations (3.20) and (3.28) gives

$$-iK_I\sqrt{\frac{a}{\pi}}\left[\frac{z}{(z^2 - a^2)^{3/2}} - \frac{\bar{z}}{(\bar{z}^2 - a^2)^{3/2}}\right] = \frac{pm}{ch\Delta}, \qquad m = 0, \pm 1, \pm 2, \ldots \tag{3.29}$$

Experimental Observations

An isotropic PMMA specimen was loaded in the testing machine as shown in figure 3.1. A plate of PMMA with dimensions 203.2x50.8x6.35mm was used. The half-length of the punch was $a = 12.1$mm. A 50mm-diameter collimated He-Ne laser beam (wave length=632nm) was employed for illumination. Two high-density gratings were positioned in the front of the specimen with the gratings parallel to the $x-$axis. Therefore information regarding the quantity $\partial(\sigma_x + \sigma_y)/\partial x$ was obtained. The grating pitch was $p = 0.0254$mm and the distance between gratings was $\Delta = 26$mm. From previous experiments it was shown that the optic constant is $c = 1\text{x}10^{-4}$mm^2/N for PMMA [2].

Figure 3.7(a) shows the expected fringe patterns described by equation (3.29) for a given P. Figure 3.7(b) shows a photograph of a real interferogram of the CGS fringes for the punch test. Note the excellent agreement between the numerical predictions and the photograph.
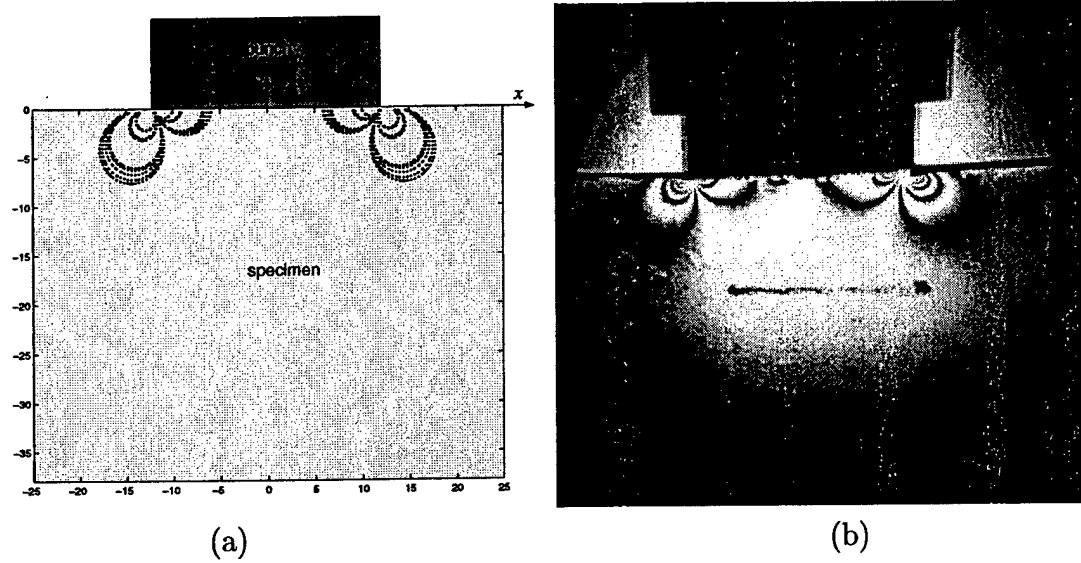
59

$$(a) \qquad\qquad\qquad (b)$$

Figure 3.7: (a) Numerical prediction of CGS fringes (constant $\partial(\sigma_x + \sigma_y)/\partial x$ values). (b) Photograph of a real interferogram of the CGS fringes. Isotropic material, transmission mode.

CGS Fringe Interpretation

To determine the stress intensity factor near the punch corner, the photograph of the CGS patterns was first digitized to obtain the fringe order (m) and fringe location at several points (x_k, y_k). Then, a least squares scheme was used to fit the experimental data from the photographs to expression (3.29) and obtain the parameter K_I.

The least squares method was developed as follows. First, define the functions

$$F_k = F(x_k, y_k) = -i\sqrt{\frac{a}{\pi}}\left[\frac{z_k}{(z_k^2 - a^2)^{3/2}} - \frac{\bar{z}_k}{(\bar{z}_k^2 - a^2)^{3/2}}\right] r_k^{3/2} \quad \text{and} \quad \alpha_k = \frac{pm_k}{ch\Delta}r_k^{3/2},$$

where $z_k = x_k + iy_k$ and $r_k = |z_k|$. Then, an attempt is made to fit the expected fringe pattern (governed by equation (3.29)) to the digitized data points by minimizing the error function

$$\psi(K_I) = \sum_{k=1}^{N}\left[F_k K_I - \alpha_k\right]^2, \qquad (3.30)$$

where N is the total number of points. Note that since there is only one parameter to be determined, i.e. K_I, this process is a very simple least squares fit. Thus, employing the

usual methods [15] it is found that

$$K_I = \frac{\sum_{k=1}^{N} \alpha_k F_k}{\sum_{k=1}^{N} F_k^2}. \tag{3.31}$$

It is noted that the function ψ weights the outer lobes of the interferograms more strongly than the inner lobes.

To assure the accuracy of using the optical CGS technique to obtain the stress intensity factor near the punch corner, the experimental CGS measurement of K_I was compared with the independently measured K_I using the measured load and equation (3.27). The result is illustrated in figure 3.8(a). The agreement between the analytical solution and the optical experimental measurement is excellent. This agreement is expected since the theoretical lobes predicted by equation (3.29) are very close to the experimental CGS fringes as noted in figure 3.8(b).

(a)   (b)
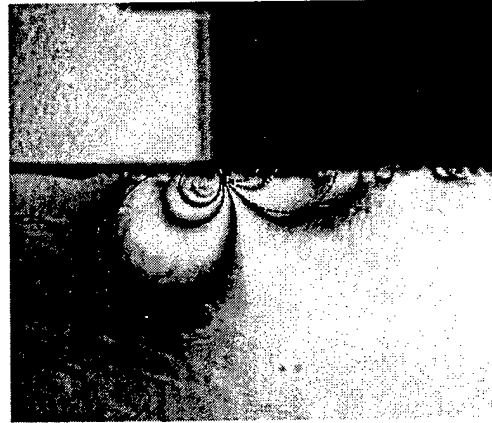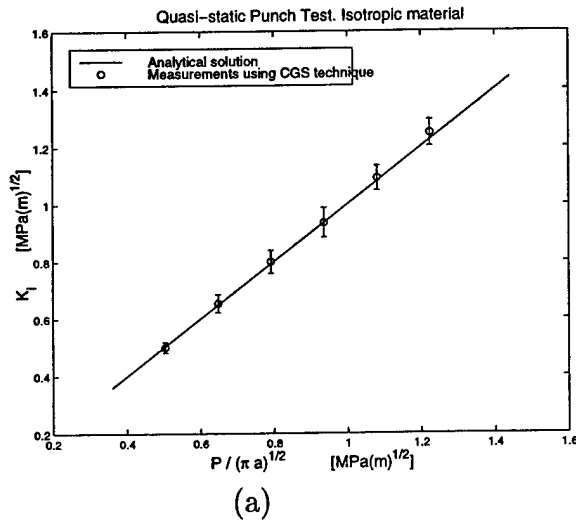
Figure 3.8: (a) Comparison of the experimental measurements of K_I with the analytical solution for the punch test with isotropic materials. (b) Comparison between predicted and observed CGS fringes.

Uncertainty Analysis

Several sources of uncertainty are involved in the experimental determination of the stress intensity factor K_I. However as will be shown below some of them are very small compared to others and can be neglected.

From standard uncertainty analysis [15], it is known that if $q(x, \ldots, z)$ is a function of several variables, then the uncertainty of q in terms of the uncertainty of the variables is given by the error propagation law

$$\delta q = \sqrt{\left(\frac{\partial q}{\partial x}\delta x\right)^2 + \ldots + \left(\frac{\partial q}{\partial z}\delta z\right)^2}, \tag{3.32}$$

for independent random errors.

The estimate for K_I given by equation (3.31) is a function of the measured numbers $\alpha_1, \ldots, \alpha_N$. Thus the uncertainty in K_I is given by simple uncertainty propagation in terms of the uncertainties in $\alpha_1, \ldots, \alpha_N$, that is

$$\delta K_I = \sqrt{\sum_{k=1}^{N}\left(\frac{\partial K_I}{\partial \alpha_k}\right)^2 \sigma_\alpha^2 + \left(\frac{\partial K_I}{\partial a}\delta a\right)^2}. \tag{3.33}$$

The first component is associated with the fitting process error and the second with the uncertainty in measuring a. It can be shown that the first component may be expressed as

$$\sum_{k=1}^{N}\left(\frac{\partial K_I}{\partial \alpha_k}\right)^2 \sigma_\alpha^2 = \frac{\sigma_\alpha^2}{\sum_{k=1}^{N} F_k^2}, \tag{3.34}$$

where

$$\sigma_\alpha = \sqrt{\frac{\psi(K_I)}{N-1}} \tag{3.35}$$

is the uncertainty in the measurements $\alpha_1, \ldots, \alpha_N$. In addition, note that

$$\frac{\partial K_I}{\partial a} = \frac{\sum_{k=1}^{N} F_k^2 \sum_{k=1}^{N}\frac{\partial F_k}{\partial a}\alpha_k - 2\sum_{k=1}^{N} F_k\alpha_k \sum_{k=1}^{N} F_k\frac{\partial F_k}{\partial a}}{\left(\sum_{k=1}^{N} F_k^2\right)^2} \tag{3.36}$$

where

$$\frac{\partial F_k}{\partial a} = \frac{1}{2a}F_k - 3ia\sqrt{\frac{a}{\pi}}\left[\frac{z_k}{(z_k^2 - a^2)^{5/2}} - \frac{\bar{z}_k}{(\bar{z}_k^2 - a^2)^{5/2}}\right]r_k^{3/2}. \tag{3.37}$$

An estimate of the uncertainty δK_I was computed according to equation (3.33), and it was found that the second component, corresponding to the uncertainty of a, was negligible in comparison with the first one, corresponding to the fitting analysis. This is due to the fact δa is much smaller than the discrepancy between the fitted and observed fringe pattern.

3.5.2 Quasi-Static Punch Problem. Orthotropic Material

Consider a rigid punch of width $2a$ acting on a half-plane of orthotropic materials. The mathematical statement of the problem is similar to that of the last subsection for the isotropic case (the boundary conditions are the same).

It can be shown [16] that the in-plane stress components for this case are

$$\sigma_x = 2\text{Re}\left\{s_1^2\phi(z_1) + s_2^2\phi(z_2)\right\} \tag{3.38}$$

$$\sigma_y = 2\text{Re}\left\{\phi(z_1) + \phi(z_2)\right\} \tag{3.39}$$

where

$$\phi(z_1) = \frac{s_2}{s_2 - s_1}g(z_1), \qquad \phi(z_2) = \frac{-s_1}{s_2 - s_1}g(z_2), \tag{3.40}$$

and

$$g(z) = \frac{-P}{2\pi\sqrt{a^2 - z^2}}, \tag{3.41}$$

with $z_1 = x + s_1 y$, $z_2 = x + s_2 y$ and s_k, $(k = 1, 2)$, being the roots of

$$a_{11}s^4 + (2a_{12} + a_{66})s^2 + a_{22} = 0. \tag{3.42}$$

The coefficients a_{ij} are related to the compliance matrix S_{ij} by

$$a_{ij} = S_{ij}$$

for plane-stress, and by

$$a_{ij} = S_{ij} - \frac{S_{i3}S_{j3}}{S_{33}} \quad (i, j = 1, 2, 4, 5, 6)$$

for plane-strain. The compliance matrix is given, in terms of engineering constants, by [17]

$$S_{11} = \frac{1}{E_1}, \qquad S_{12} = \frac{-\nu_{12}}{E_1}, \qquad S_{44} = \frac{1}{\mu_{23}},$$

$$S_{22} = \frac{1}{E_2}, \qquad S_{13} = \frac{-\nu_{13}}{E_1}, \qquad S_{55} = \frac{1}{\mu_{13}},$$

$$S_{33} = \frac{1}{E_3}, \qquad S_{23} = \frac{-\nu_{23}}{E_2}, \qquad S_{66} = \frac{1}{\mu_{12}}.$$

From the Generalized Hooke's law for orthotropic materials it can be shown that

$$\epsilon_z = S_{13}\sigma_x + S_{23}\sigma_y + S_{33}\sigma_z. \tag{3.43}$$

For a thin plate specimen, it is assumed that plane-stress deformation conditions prevail and $\sigma_z = 0$. Also, according to the generalized plane-stress assumption, ϵ_z is assumed uniform through the specimen thickness and the out-of-plane surface displacement $w(x, y)$ can be related to the in-plane stress components through

$$w(x, y) = \frac{1}{2} \int_{-h/2}^{h/2} \epsilon_{33} \, dz = \frac{h}{2} \left\{ S_{13}\sigma_x + S_{23}\sigma_y \right\}. \tag{3.44}$$

Taking the derivative of this equation with respect to x and in light of (3.38) and (3.39) we get

$$\frac{\partial w}{\partial x} = K_I \frac{h}{2} \sqrt{\frac{a}{\pi}} \mathrm{Re} \left\{ \frac{s_2}{s_1 - s_2} \frac{z_1(S_{13}s_1^2 + S_{23})}{(a^2 - z_1^2)^{3/2}} - \frac{s_1}{s_1 - s_2} \frac{z_2(S_{13}s_2^2 + S_{23})}{(a^2 - z_2^2)^{3/2}} \right\} \tag{3.45}$$

where $K_I = P/\sqrt{\pi a}$ has been used. Finally the equation governing the CGS fringes for the quasi-static punch test in orthotropic materials may be derived. For the reflection mode, combining (3.22) and (3.45) gives

$$K_I \frac{h}{2} \sqrt{\frac{a}{\pi}} \mathrm{Re} \left\{ \frac{s_2}{s_1 - s_2} \frac{z_1(S_{13}s_1^2 + S_{23})}{(a^2 - z_1^2)^{3/2}} - \frac{s_1}{s_1 - s_2} \frac{z_2(S_{13}s_2^2 + S_{23})}{(a^2 - z_2^2)^{3/2}} \right\} = \frac{mp}{2\Delta} \tag{3.46}$$

where $m = 0, \pm 1, \pm 2, \ldots$. Figure 3.9 shows the expected CGS fringe patterns described by this equation for a given K_I and the material properties given in table 3.1.

Experimental observations and fringe interpretation

The procedure to experimentally examine the composite material was similar to that used in the isotropic punch test. The dimensions of the specimen were 100x50x6.3 mm. The half-width of the punch was $a = 15$ mm. The x gradient was considered, i.e., $\partial w/\partial x$ was measured. The distance between gratings was $\Delta = 44$mm. Figure 3.10 shows a photograph of the fringe pattern observed in the composite with fibers parallel to the x−axis. Note the similarity between the numerical predictions, figure 3.9, and the fringes observed, figure 3.10.
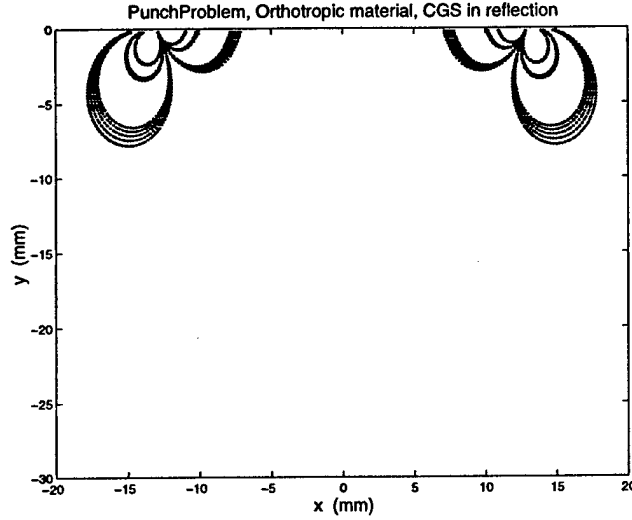
64

Figure 3.9: Numerical prediction of the CGS fringes, $\partial w/\partial x$, for the punch test in composite materials with fibers parallel to the $x-$axis.
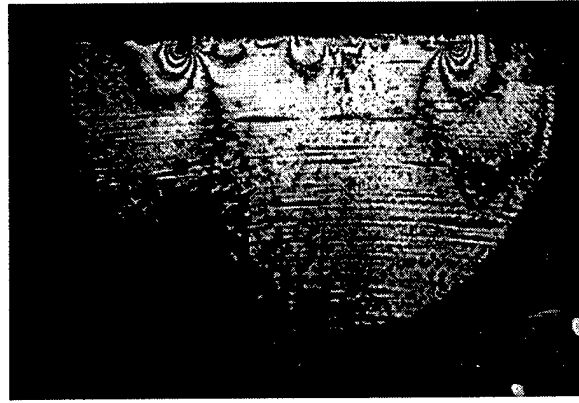

Figure 3.10: Photograph of a real interferogram of the CGS fringes. Composite material with fibers parallel to the $x-$axis.

As in the isotropic case, the least square scheme was used to fit the experimental data from the photographs to expression (3.46) to find the parameter K_I. The results are shown in figure 3.11, where a good comparison between the experimental measurements and the analytical expression for K_I is observed.

An estimate of the uncertainty δK_I was computed for the orthotropic case. From the error propagation law and neglecting the uncertainty δa we have

$$\delta K_I = \sqrt{\sum_{k=1}^{N}\left(\frac{\partial K_I}{\partial \alpha_k}\right)^2 \sigma_\alpha^2 + \left(\frac{\partial K_I}{\partial s_1}\delta s_1\right)^2 + \left(\frac{\partial K_I}{\partial s_2}\delta s_2\right)^2}. \tag{3.47}$$

65
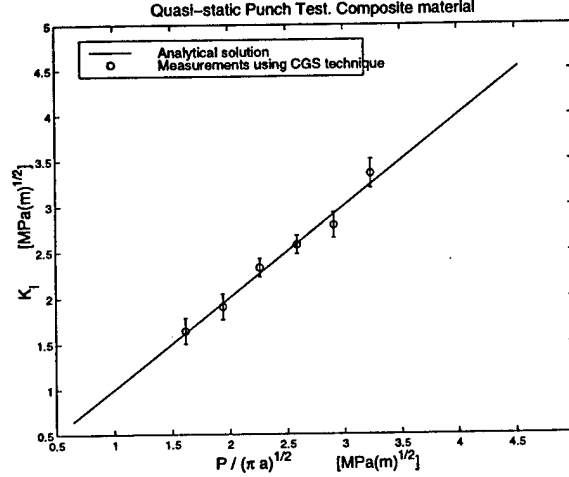
Figure 3.11: Comparison of the CGS experimental measurements with the analytical solution for the punch test in composite materials.

The first component is given by (3.34) but with the proper definition of F_k and α_k. The second and third components are much more complicated though. Note, for example, that

$$\frac{\partial K_I}{\partial s_1} = \frac{\sum_{k=1}^{N} F_k^2 \sum_{k=1}^{N} \frac{\partial F_k}{\partial s_1} \alpha_k - 2 \sum_{k=1}^{N} F_k \alpha_k \sum_{k=1}^{N} F_k \frac{\partial F_k}{\partial s_1}}{\left(\sum_{k=1}^{N} F_k^2\right)^2} \tag{3.48}$$

depends on $\partial F_k / \partial s_1$ and this depends on δs_1 which depends on the uncertainty of the material properties E_1, E_2, μ_{12} and ν_{12}. Similarly $\partial F_k / \partial s_2$ and δs_2 depend on E_1, E_2, μ_{12} and ν_{12}.

The three components of the uncertainty in (3.47) were calculated. However it was found that the second and third components are two orders of magnitude smaller than the first one. The first component, due to the fitting process, is the dominant factor in the uncertainty.

3.6 Dynamic Punch Test

The dynamic punch test was conducted on PMMA and graphite epoxy composites. The specimen was impacted on one side by a rigid projectile made of hardened steel as shown schematically on figure 3.12.

3.6.1 Isotropic Materials

Experimental Procedure

The stress intensity factor for dynamic tests was examined experimentally. The specimen geometry is shown in figure 3.12. Specimens are made of PMMA; the mechanical properties are given in table 3.3. Impact of the specimen is achieved by a cylindrical steel projectile shot by an air gun as shown schematically in figure 3.13. The apparatus consists primarily of an air gun, a Cordin 330 high speed camera and a coherent argon-ion laser pulsed for 10ns. Once the projectile is launched it travels along the barrel and activates two infrared detectors placed on the barrel close to the specimen. The signal from the detectors triggers the camera and laser controllers. A combination of delay generators make it possible to take pictures at the exact impact time. A pulse counter limits the laser to only 80 pulses of 10 ns each, giving 80 images per test. The velocity of the projectile, V_p, is determined by recording the time it takes to cross the infrared detectors. The speed of the camera was set to $5.2\mu s$ between pictures or 192,300 frames/sec.
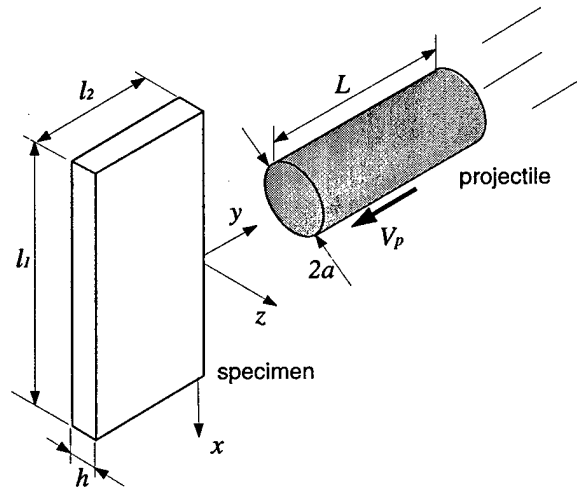
Figure 3.12: Specimen and projectile geometry in the dynamic punch test.

Three tests were performed using different specimen/punch dimensions. In all the cases the thickness of the PMMA plates was 6.3mm, the grating pitch was $p = 0.0254$ mm, the distance between gratings was $\Delta =30$ mm, and a 50 mm-diameter collimated laser beam

Table 3.3: Mechanical properties for PMMA

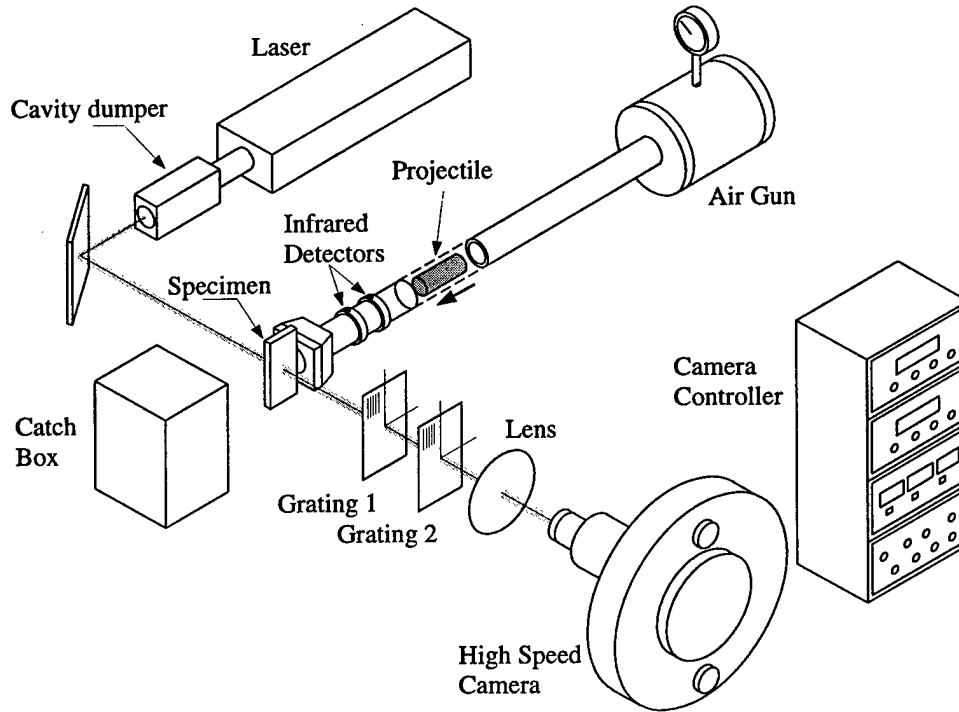| E (GPa)	3.39 ±0.05
ν	0.3 ±0.01
c (mm^2/N)	1e-4
$c_d^{pl-\sigma}$ (m/s)	1904 ±15
ρ (Kg/m^3)	1190 ±10

Figure 3.13: Schematic illustration of CGS set-up in transmission mode for use in the dynamic punch test.

was used. The first experiment was conducted on a plate with dimensions (see figure 3.12), l_1 =127 mm, l_2 =50.8 mm and a projectile with length L =145 mm and $2a$ =25.4 mm. In this case the projectile impacted the specimen at the velocity V_p =16 m/s. For the second test l_1 =100 mm, l_2 =30 mm, L =145 mm, $2a$ =30 mm and V_p =18.5 m/s. For the third test l_1 =177 mm, l_2 =50 mm, L =304 mm, $2a$ =30 mm and V_p =16 m/s.

Experimental Results

Figure 3.14 shows a series of some CGS interferograms for the first test. Note that the size of the lobes increases and then decreases with time. Such a behavior is expected for the

stress intensity factor as well. An analysis of each photograph was performed by means of procedure similar to that used in the quasi-static case. This lead to the determination of the time evolution of the stress intensity factor $K_I(t)$ for the punch test.
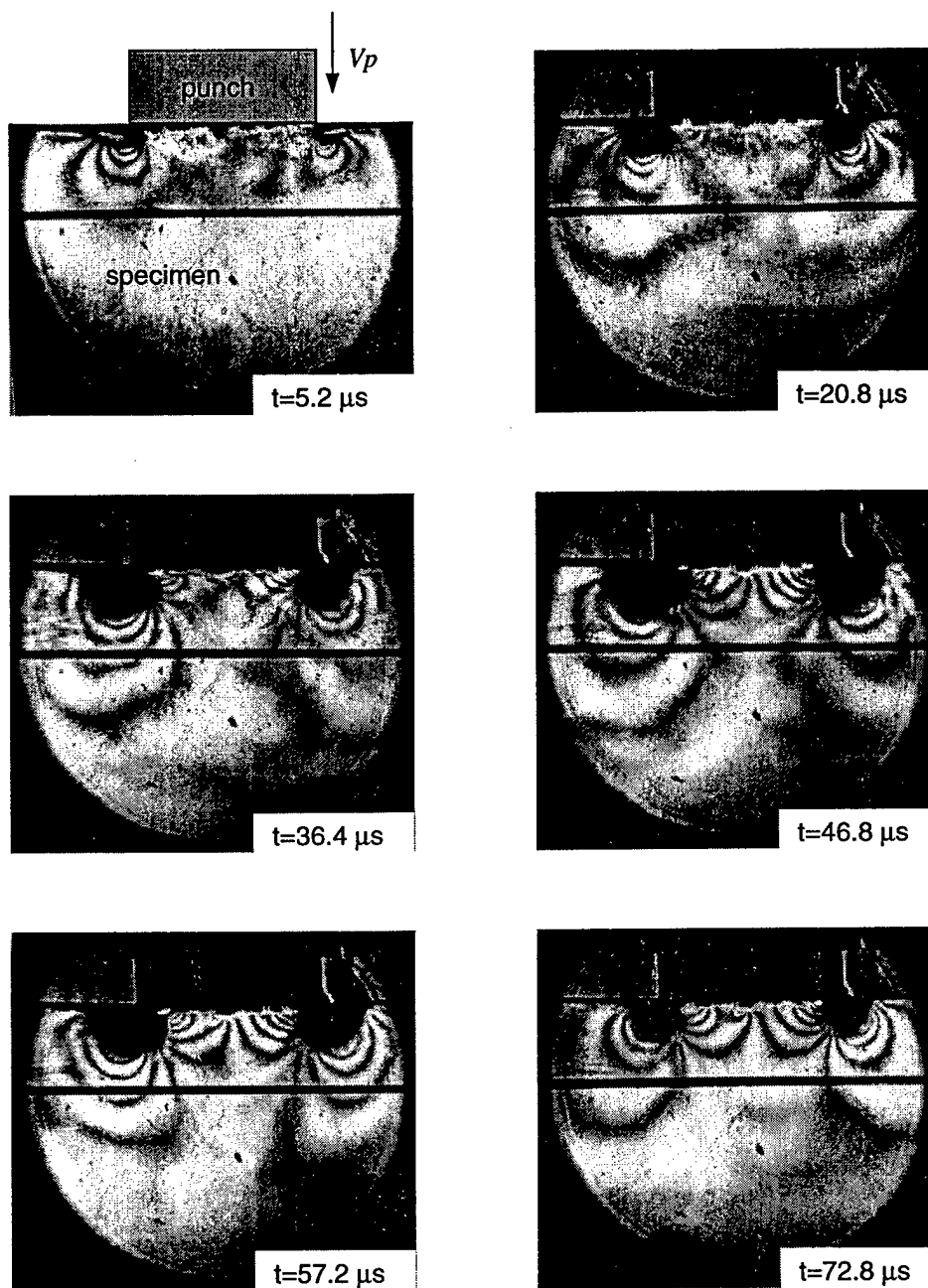

Figure 3.14: Sequence of CGS interferograms for the dynamic punch test. Transmission mode, isotropic materials.

Figure 3.15 shows a good agreement between experimental CGS fringe pattern and the

numerical reconstruction from the one term fitting procedure. The time evolution $K_I(t)$ is shown in figure 3.16 for the first experiment. The normalization factor is $K_0 = \sigma_0 C_I \sqrt{2a/c_d}$, where C_I is a material dependent parameter given in equation (3.9) and $\sigma_0 = \rho c_d V_p$. The mass density ρ and the dilatational wave speed c_d for PMMA are given in table 3.3. The particular feature for this experiment is that the pulse duration (as determined by the length of the projectile) is less than the time needed for the dilatational waves to reflect from the specimen boundaries and reach the punch corners. As discussed in section 2, the dynamic stress intensity factor for the semi-infinite punch under impact load $\sigma_0 H(t)$ applied during a time interval $0 < t < t^*$ (equation (3.10)) is

$$K_I(t) = \sigma_0 C_I \left[\sqrt{t} H(t) - \sqrt{t - t^*} H(t - t^*) \right] \tag{3.49}$$

where C_I is a material dependent parameter. For the isotropic case in mode I loading [11]

$$C_I = 4 \frac{c_s}{c_d} \sqrt{c_d (1 - c_s^2/c_d^2)/\pi}. \tag{3.50}$$

Note in equation (3.49) that the stress intensity factor $K_I(t)$ due to a pulse $\sigma_0 H(t)$ of duration t^* is equivalent to considering two semi-infinite pulses with the second applied after the time t^* and of opposite sign making $K_I(t)$ decrease. In the experimental situation, after the punch impacts the specimen, a compressive dilatational wave propagates through the specimen, and since the boundaries are stress free, the reflected wave from the opposite side is tensile such that when it arrives at the punch corners it makes $K_I(t)$ decrease. The decay of $K_I(t)$ in both cases is compared in figures 3.16-3.18.

A plot of equation (3.49) is shown in figure 3.16 by the solid line. The pulse duration is $t^* = 49.4 \mu s$ which is the time for the dilatational wave to travel twice the punch length, the normalized time is $c_d t^*/2a = 3.35$. Note that c_d denotes the dilatational wave speed of the specimen which is different from that of the projectile since they are made of different materials. A good agreement is observed between the solid line and the experimental results. The increase and beginning of decrease of $K_I(t)$ is noted in the experimental results. The solid line assumes a semi-infinite plate solution, i.e., it does not consider wave reflections
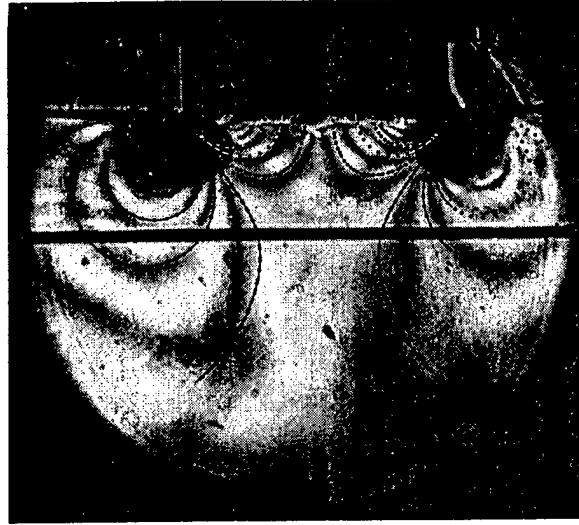
Figure 3.15: Comparison between experimental CGS interferogram and numerical simulation reconstructed from one term analysis.

from boundaries. It should be noted that the comparison of the experimental results is made against the semi-infinite punch solution (or semi-infinite crack). Although in the experiments the punch width is finite, it has been observed [6] that the effect of the scattered waves from the punch corners is minimum.

Figure 3.17 shows the dynamic stress intensity factor for the second experiment. Note again a good agreement in the loading zone between experimental results and the theoretical prediction for the semi-infinite punch. After the normalized time $c_d t/2a = 2$, decay occurs on $K_I(t)$ due to the arrival at the punch corners of the reflected waves from the side of the specimen opposite to the side impacted by the punch.

The third experiment is similar to the second test in the sense that the decay of $K_I(t)$, at normalized time $c_d t/2a = 3.33$, is due to the arrival at the punch corners of the reflected waves from the opposite side of the specimen, figure 3.18. Due to the specimen/punch dimensions for this experiment, the length of the pulse $c_d t^*/2a = 5.93$ is long enough such that it does not affect the behavior of $K_I(t)$, i.e., it does not contribute to the decay of $K_I(t)$ as in the first experiment.

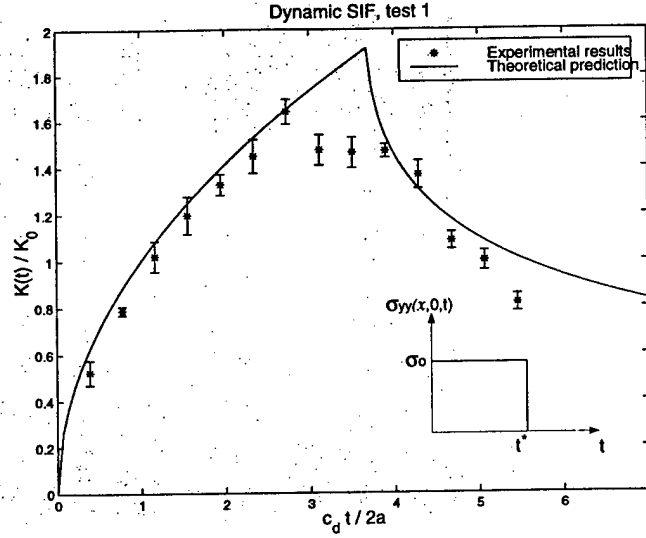The uncertainty analysis for this case requires one to estimate $\delta\left(\frac{K_I}{K_0}\right)$, that is, the un-

Figure 3.16: Normalized dynamic stress intensity factor for the punch test. First test, short pulse duration.

certainty of the normalization factor K_0 should be considered in the expression

$$\delta \left(\frac{K_I}{K_0} \right) = \sqrt{ \left(\frac{\delta K_I}{K_0} \right)^2 + \left(\frac{K_I}{K_0^2} \delta K_0 \right)^2 }.$$

δK_I is determined as in the quasi-static punch problem. Neglecting the uncertainty δa we found from the definition of K_0 that

$$\delta K_0 = \sqrt{ \left(C_I \sqrt{\frac{2a}{c_d}} \delta \sigma_0 \right)^2 + \left(\sigma_0 \sqrt{\frac{2a}{c_d}} \delta C_I \right)^2 + \left(\frac{\sigma_0 C_I \sqrt{2a}}{2 c_d^{3/2}} \delta c_d \right)^2 }.$$

A successive application of the error propagation law is needed to express $\delta \sigma_0$, δC_I and δc_d in terms of the uncertainty of the material properties. After the proper calculation it was found that that $\delta \left(\frac{K_I}{K_0} \right)$ is different from $\frac{\delta K_I}{K_0}$ by less than 5%, which means that that the uncertainty in the normalization factor may be neglected. Again, the largest, dominant uncertainty is that due to the fit.

3.6.2 Orthotropic Materials

Experimental Procedure

The dynamic punch test was conducted on unidirectional fiber-reinforced composite materials to measure the time evolution of the stress intensity factor $K_I(t)$. The graphite-epoxy
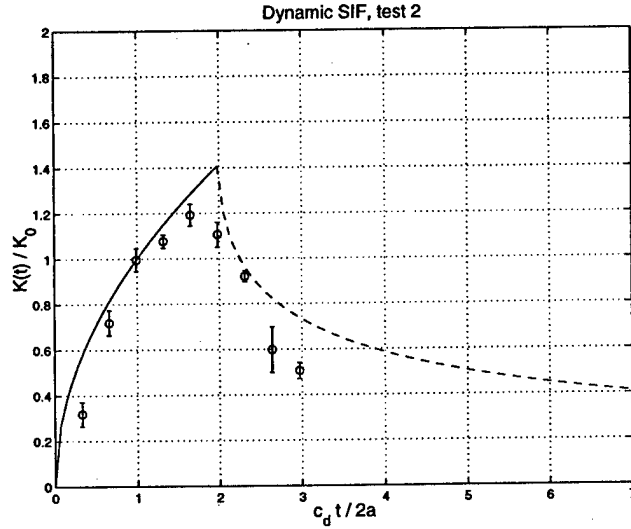
Figure 3.17: Normalized dynamic stress intensity factor for the punch test. Second test.

composite used in the dynamic experiments is the same as that employed in the quasi-static test, and the relevant properties are given in tables 3.1 and 3.2.

The CGS set-up in reflection for the dynamic punch test is shown schematically in figure 3.19. Note the addition of the beam splitter and the different laser beam path with respect to the set-up for transmission mode, figure 3.13.

With reference to the figure 3.12, the dimensions of the specimen/projectile used in the test are $l_1 = 101.6$mm, $l_2 = 50.8$mm, $h = 6.5$mm, $L = 304$mm, $2a = 30$mm. The fiber orientation of the specimen was along the x−axis. The x−gradient was considered, i.e., $\partial w/\partial x$ was measured. The projectile impacted the specimen at the velocity $V_p = 11.5$m/s. The grating pitch was $p = 0.0254$mm and the distance between gratings was $\Delta = 36$mm. The speed of the camera was set to 4μs between pictures or 250,000 frames/sec.

Experimental Results

A sequence of pictures displaying the CGS fringe pattern for the dynamic punch test in composites is shown in figure 3.20. An analysis of each photograph was performed by means of a similar procedure to that used in the quasi-static case for composites, and thus, the stress intensity factor time evolution $K_I(t)$ is determined.
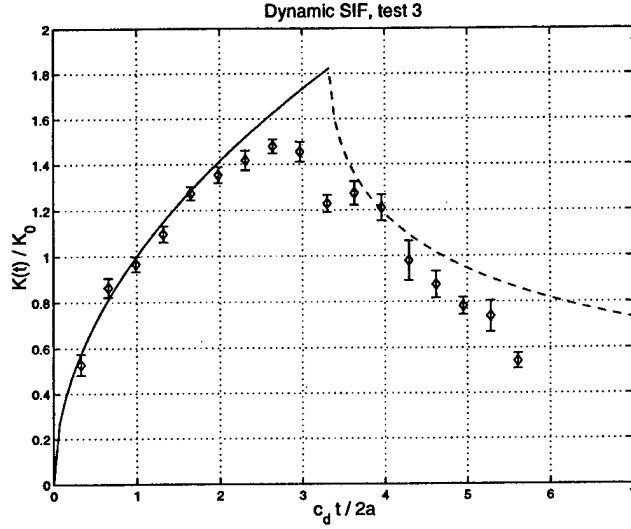
Figure 3.18: Normalized dynamic stress intensity factor for the punch test. Third test.

A comparison between the experimental CGS fringes and the numerical reconstruction from the one term fitting procedure is shown in figure 3.21, note the good agreement in both sets of fringes. The normalized dynamic stress intensity factor for the punch test is shown in figure 3.22. The normalization factor is $K_0 = \sigma_0 C_I \sqrt{2a/c_{d,y}}$, where $\sigma_0 = \rho c_{d,y} V_p$, being $c_{d,y}$ the dilatational wave speed for wave propagation along the $y-$axis and is given in table 3.2. The normalized time is $c_{d,y}t/2a$. An increase in $K_I(t)$ is noted and then a decrease occurs when the dilatational wave reflected from the opposite side of the specimen arrives at the punch corners. The solid line corresponds to the stress intensity factor for the semi-infinite punch problem under impact load $\sigma_0 H(t)$ applied during a time interval $0 < t < t^*$ (equation (3.10))

$$K_I(t) = \sigma_0 C_I \left[\sqrt{t} H(t) - \sqrt{t - t^*} H(t - t^*) \right] \tag{3.51}$$

where C_I is a material dependent parameter derived by Rubio-Gonzalez and Mason [10] and given in equation (3.8),

$$C_I = 2 \sqrt{\frac{2 c_s \xi}{\pi \sqrt{c_{22}}}}. \tag{3.52}$$

The uncertainty $\delta\left(\frac{K_I}{K_0}\right)$ was estimated following the procedure described for the dynamic punch test in isotropic materials. Again it was found that $\delta\left(\frac{K_I}{K_0}\right)$ is not very different from
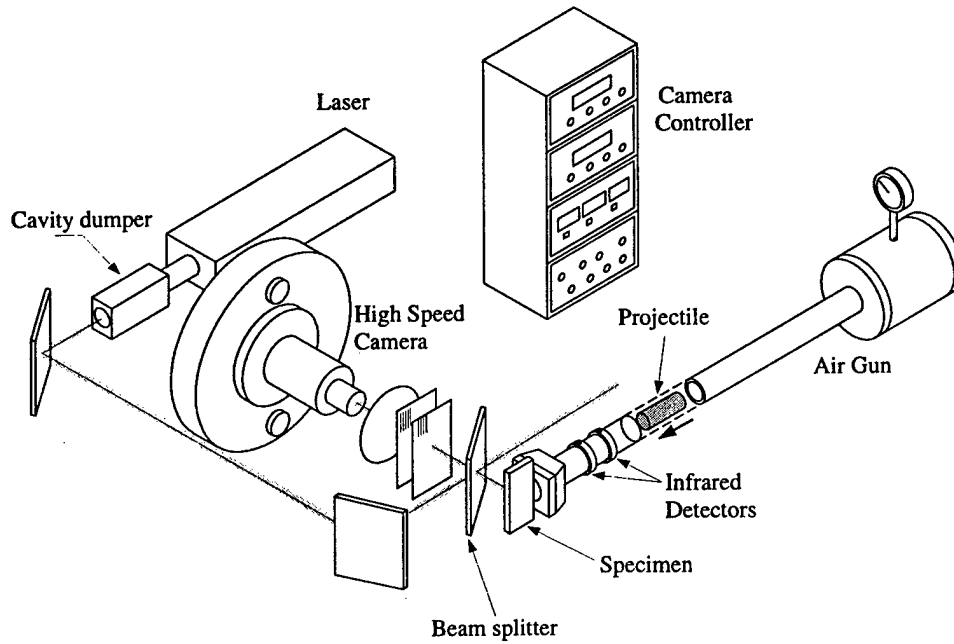
74

Figure 3.19: Schematic illustration of CGS set-up in reflection mode for use in the dynamic punch test of composites.

$\frac{\delta K_I}{K_0}$, i.e., the uncertainty in the normalization factor can be neglected.

3.7 Conclusions

Like in dynamic fracture mechanics, the dynamic stress intensity factor K_I has been introduced to characterize the severity of the singular stresses around the punch corners in the punch test. Quasi-static and dynamic punch tests were performed on PMMA and unidirectional graphite-epoxy composites to measure K_I. Laser interferometry was used to measure in-plane stresses (transmission mode) and out-of-plane displacements (reflection mode), and then estimate the stress intensity factor. In the dynamic case, a high speed photography technique was employed to capture the transient response of the specimen and measure $K(t)$ just after the impact. Each photograph of the CGS fringe pattern was digitized. A fitting procedure based on the least squares method was used to estimate K_I from the fringe pattern. In all the cases a good agreement between the measurements of K_I and the theoretical predictions was found. The theoretical prediction for the dynamic case on composites is just
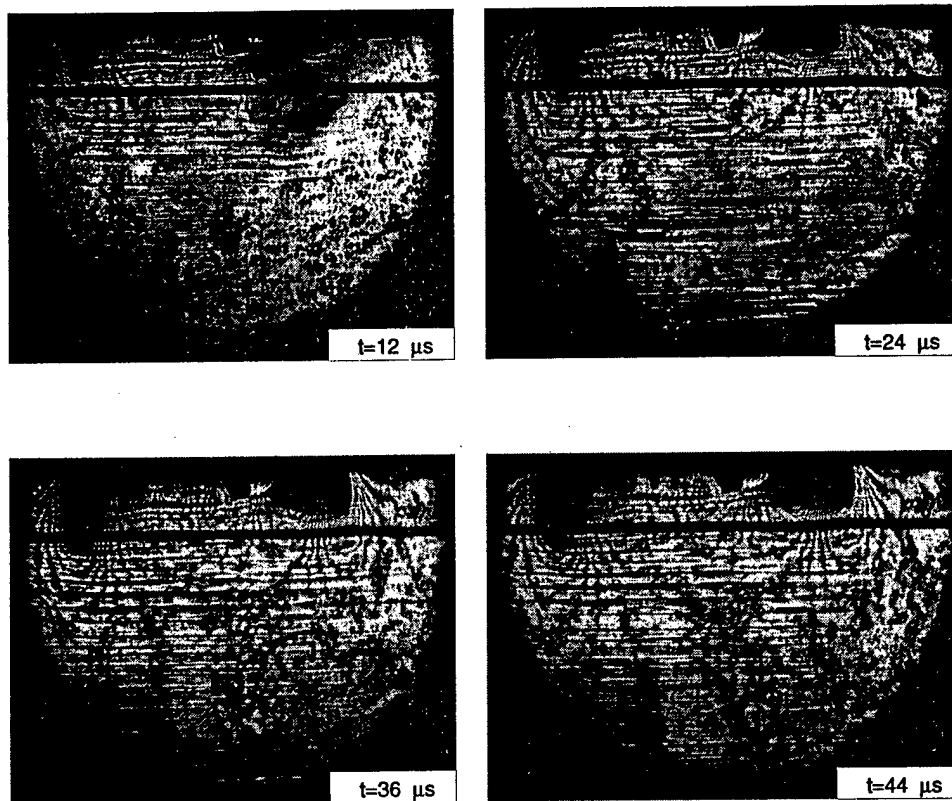
75

Figure 3.20: Sequence of CGS interferograms in reflection for the dynamic punch test in composites.

an extension of the solutions developed for orthotropic materials. [6, 10]

An estimate of the uncertainty in the experimental determination of K_I was made. It was found that the dominant contribution to the uncertainty δK_I was that associated with the fitting procedure.
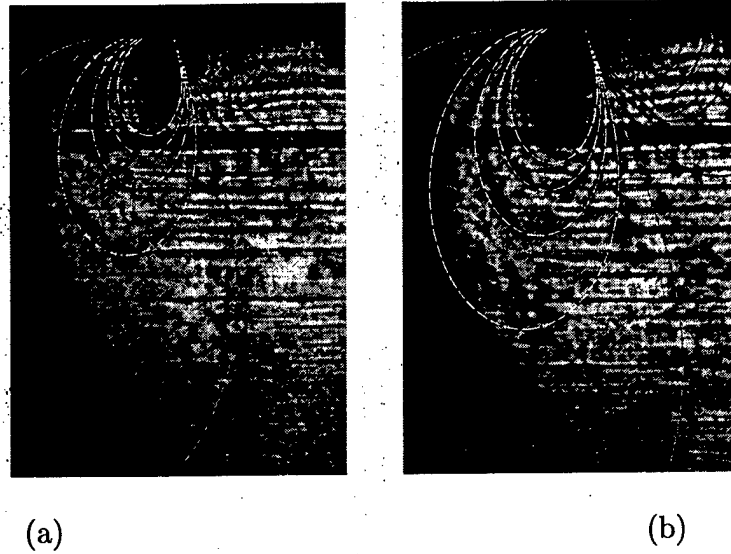
(a)   (b)

Figure 3.21: Experimental CGS interferograms and numerical simulation reconstructed from one term fitting analysis. Composite materials. (a) At $t = 12\mu s$ and (b) at $t = 20\mu s$.
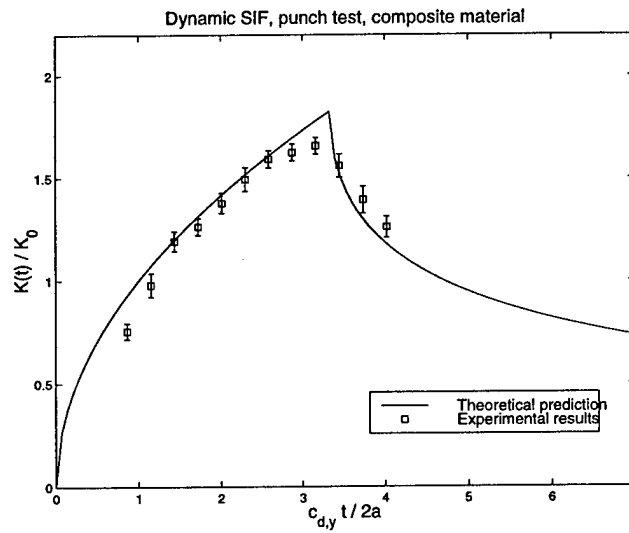

Figure 3.22: Normalized dynamic stress intensity factor for the punch test. Composite materials

Bibliography

[1] H. Tippur, S. Krishnaswamy, and A. Rosakis. A coherent gradient sensor for crack tip measurements: Analysis and experimental results. *Int. J. fracture*, 48:193–204, 1991.

[2] J. Mason, J. Lambros, and A. Rosakis. The use of a coherent gradient sensor in dynamic mixed-mode fracture mechanics experiments. *J. Mech. Phys. Solids*, 40(3):641–661, 1992.

[3] J. Lambros and A. Rosakis. Dynamic crack initiation and growth in thick unidirectional craphite/epoxy plates. *Composites Sci. and Tech.*, 57:55–65, 1997.

[4] J. Lambros and A. Rosakis. An experimental study of dynamic delamination of thick fiber reinforced polymeric matrix composites. *Experimental Mechanics*, 37(3):360–366, 1997.

[5] C. Liu, A. J. Rosakis, R. W. Ellis, and M. G. Stout. A study of the fracture behavior of unidirectional fiber-reinforced composites using coherent gradient sensing interferometry. *Int. J. Fracture*, 90(4):355–382, 1998.

[6] C. Rubio-Gonzalez. *Dynamic Fracture Initiation in Composite Materials*. PhD thesis, University of Notre Dame, 1999.

[7] K. L. Johnson. *Contact Mechanics*. Cambridge University Press. New York, NY, 1987.

[8] G. M. Gladwell. *Contact Problems in the Classical Theory of Elasticity*. Sijthoff and Noordhoff. The Netherlands, 1980.

[9] K. Roessig and J. Mason. Dynamic stress intensity factors in the dynamic punch test. *Eng. Fracture Mech.*, 60(4):421–435, 1998.

[10] C. Rubio-Gonzalez and J. Mason. Dynamic stress intensity factors at the tip of a uniformly loaded semi-infinite crack in an orthotropic material. *Accepted in J. Mech. Phys. Solids*, 1999c.

[11] L. B. Freund. *Dynamic Fracture Mechanics*. Cambridge University Press. New York, NY, 1990.

[12] J. Mason, A. Rosakis, and G. Ravichandran. Full field measurements of the deformation field around a growing adiabatic shear band at the tip of a dynamically loaded notch. *J. Mech. Phys. Solids*, 42(11):1679–1697, 1994.

[13] D. Post, B. Han, and P. Ifju. *High Sensitivity Moiré. Experimental Analysis for Mechanics and Materials*. Springer-Verlag. New York, NY, 1994.

[14] N. I. Muskhelishvili. *Some Basic Problems in the Mathemathical Theory of Elasticity*. Noordhoff, Groningen, Holland, 1953.

[15] J. R. Taylor. *An Introduction to Error Analysis*. University Science Books, Oxford University Press. Mill Valley, CA, 1982.

[16] A. E. Green and W. Zerna. *Theoretical Elasticity*. Dover Publications Inc. New York, NY, 1992.

[17] R. M. Jones. *Mechanics of Composite Materials*. Taylor and Francis. New York, NY, 1975.

REPORT DOCUMENTATION PAGE

1. AGENCY USE ONLY (Leave blank)	2. REPORT DATE JAN 31 2000	3. REPORT TYPE AND DATES COVERED Final Report, 01 JUN 96/31 DEC 99

4. TITLE AND SUBTITLE

Applications of Dynamic Fracture Mechanics Concepts to Composites: Final Report 2000

5. FUNDING NUMBERS

G:N00014-96-1-0774

6. AUTHOR(S)

J.J. Mason

7. PERFORMING ORGANIZATION NAMES(S) AND ADDRESS(ES)

University of Notre Dame
Notre Dame, IN 46556

8. PERFORMING ORGANIZATION REPORT NUMBER

Structural/Solid Mechanics
00/1

9. SPONSORING / MONITORING AGENCY NAMES(S) AND ADDRESS(ES)

Office of Naval Research
Ship Structures Division (ONR 334)
800 N Quincy St
Arlington VA 22217

10. SPONSORING / MONITORING AGENCY REPORT NUMBER

11. SUPPLEMENTARY NOTES

a. DISTRIBUTION / AVAILABILITY STATEMENT

Approved for Public Release

12. DISTRIBUTION CODE

13. ABSTRACT (Maximum 200 words)

This report summarizes the work completed in the months of June 1996 – December 1999 for the principal investigator's Young Investigator Program grant. As such, the report represents a final summary of work, organized as follows. First, in a brief summary chapter, a review of the accomplishments of the work supported from June 1996 to December 1999 is given providing an overview of the successes during that period. Next, two chapters giving details of new work during the six months since the last annual report are presented. In these results, an experimentally useful solution for the stress intensity factor history at the corner of an impacting punch is derived for isotropic and orthotropic materials. Then that solution is compared to experimental measurements of the stress intensity factor history at the corner of an impacting punch in both isotropic and anisotropic materials. Good agreement between model and experiments is seen. Consequently, it is concluded that the solutions derived throughout the duration of this work are accurate – mathematically speaking the fundamental solutions are exact – and describe the loading under blunt impact quite well. With such accurate descriptions of the stress in the material under impact, future work can now focus on understanding the failure in the material under these same conditions.

14. SUBJECT TERMS

Stress Intensity Factor, Dynamic Fracture, Orthotropic Materials, Punch Impact

15. NUMBER OF PAGES

79

16. PRICE CODE

17. SECURITY CLASSIFICATION OF REPORT	18. SECURITY CLASSIFICATION OF THIS PAGE	19. SECURITY CLASSIFICATION OF ABSTRACT	20. LIMITATION OF ABSTRACT
Unclassified	Unclassified	Unclassified	